

A unified cross-attention model for predicting antigen binding specificity to both HLA and TCR molecules

Received: 25 April 2024

Chenpeng Yu , Xing Fang, Shiye Tian & Hui Liu  

Accepted: 11 December 2024

Published online: 28 January 2025

 Check for updates

The immune checkpoint inhibitors have demonstrated promising clinical efficacy across various tumour types, yet the percentage of patients who benefit from them remains low. The bindings between tumour antigens and human leukocyte antigen class I/T cell receptor molecules determine the antigen presentation and T cell activation, thereby playing an important role in the immunotherapy response. In this paper, we propose UnifyImmun, a unified cross-attention transformer model designed to simultaneously predict the bindings of peptides to both receptors, providing more comprehensive evaluation of antigen immunogenicity. We devise a two-phase strategy using virtual adversarial training that enables these two tasks to reinforce each other mutually, by compelling the encoders to extract more expressive features. Our method demonstrates superior performance in predicting both peptide-HLA and peptide-TCR binding on multiple independent and external test sets. Notably, on a large-scale COVID-19 peptide-TCR binding test set without any seen peptide in the training set, our method outperforms the current state-of-the-art methods by more than 10%. The predicted binding scores significantly correlate with the immunotherapy response and clinical outcomes on two clinical cohorts. Furthermore, the cross-attention scores and integrated gradients reveal the amino acid sites critical for peptide binding to receptors. In essence, our approach marks an essential step towards comprehensive evaluation of antigen immunogenicity.

Immune checkpoint inhibitors have already demonstrated effective clinical antitumour efficacy in various types of tumours¹. However, the percentage of patients who benefit from immunotherapy remains limited. A number of studies have confirmed that tumour antigens (neoantigens) play a crucial role in the immunotherapy response^{2,3}. In fact, the anticancer immune response involves a sequence of intricate biological events that lead to effective killing of cancer cells. Initially, tumour antigens are released by cancer cells through a specific mechanism, and are captured and processed by antigen-presenting cells⁴. These antigen-presenting cells present the neoantigens on their outer

cell surface (antigen presentation). Only if naive T cells recognize the antigenic epitopes and bind to the peptide-HLA (pHLA) complex can they be conditionally activated and subsequently differentiate into effector T cells, such as cytotoxic T lymphocytes^{2,5-8}. The effector T cells migrate to the tumour site and attack cancer cells⁹, ultimately inducing their death¹⁰. These steps are referred to as the cancer-immunity cycle¹¹, which indeed highlights a delicate balance between the recognition of non-self antigens and the prevention of autoimmunity. Within this process, antigen presentation and T cell activation stand out as two steps critical to the success of the anticancer immune response^{12,13}.

The binding of peptides to human leukocyte antigen (HLA) class I molecules is a fundamental step for neoantigen presentation¹². HLA alleles are well-known for their high specificity and polymorphism in the human population¹⁴, leading to the restrictive binding of a narrow range of peptides¹⁵. Following antigen presentation, the recognition of the presented antigens by T cell receptors (TCRs) is another crucial step to elicit T cells¹⁵. This step is also highly selective, allowing only a small portion of antigens that can be recognized and bound by TCRs. This selectivity, known as TCR binding specificity, arises from the high diversity of the TCR repertoire (estimated to range from 10^{15} to 10^{64} possible receptors in humans)¹⁶. This diversity is primarily manifested in the complementarity determining region 3 (CDR3)¹⁷, which directly interacts with the pHLA complex and determines the TCR binding specificity^{18,19}. The binding specificity ensures that only the immunogenic neoantigens can trigger immune response, thereby maintaining the delicate balance between effective immune responses and autoimmune reactions.

The HLA polymorphism and TCR diversity represent the evolutionarily acquired traits that enable the human immune system to respond to a wide array of pathogens at the individual level^{20,21}. Some experimental assays such as mass spectrometry-eluted HLA ligands²², and techniques such as single-cell TCR sequencing²³ and T-scan²⁴, have been developed to detect pHLA and peptide-TCR (pTCR) bindings, respectively. However, these experimental assays are often time-consuming, technically complex and costly. To address these challenges, some computational methods have emerged as viable alternatives to predict peptide-receptor bindings²⁵. The pHLA prediction methods include TransPHLA²⁶, MHCflurry²⁷, NetMHCpan4.0 (ref. 28), DeepLigand²⁹ and BERTMHC³⁰. The pTCR prediction methods include PanPep³¹, pMTnet³², DLpTCR³³, ERGO2 (ref. 34), TITAN³⁵ and ATMTCR³⁶. The ImmRep 2022 TCR-epitope specificity workshop released a dataset to benchmark the performance of more than ten predictive methods for pTCR bindings³⁷. Although current methods have demonstrated promising predictive accuracy, they primarily focus on the prediction of pHLA or pTCR binding alone. However, the immunogenicity of antigens is actually influenced by the binding affinity to both HLA and TCR molecules, rather than just one.

Distinct from previous studies that consider pHLA or pTCR binding specificity alone, we propose a unified model, UnifyImmun, which integrates the predictive tasks of pHLA and pTCR bindings to establish a one-stop deep learning framework for comprehensive evaluation of antigen immunogenicity. UnifyImmun comprises three blocks: sequence embedding, encoder and cross-attention (Fig. 1a). The sequence embedding block receives the HLA, peptide and TCR sequences as inputs, and respectively maps them into embeddings in latent space. Three self-attention encoders share a common network structure, but operate with independent parameters to extract expressive features from three types of sequence embeddings, respectively. Next, two cross-attention layers are introduced to effectively fuse the features of the peptide-HLA pairs and peptide-TCR pairs, respectively. The output of the cross-attention layers is passed through fully connected layers and softmax transformation to yield predictions for pHLA and pTCR binding, respectively. Particularly, the cross-attention scores offer valuable insights into the crucial amino acids and positional preference in peptides for binding to HLA and TCR molecules ('Cross-attention scores reveal critical peptide sites').

Given the vast diversity of HLA and TCR repertoires, the experimentally validated bindings currently available are limited and even biased, posing a tough challenge of overfitting in the development of a prediction model. To overcome this limitation, we have introduced virtual adversarial training as a means to improve the model generalizability ('Virtual adversarial training'). Specifically, we apply adversarial perturbations to the sequence embeddings to generate virtual adversaries that aim to maximize the loss function. The adversarial training makes our model less sensitive to slight changes in input sequences,

and thereby significantly improves the performance ('Model ablation experiments').

Ideally, our model prefers to be trained using HLA-peptide-TCR triplet samples. However, the availability of such triplets is currently limited, whereas pHLA and pTCR pairwise bindings are relatively abundant (Fig. 1c,d and Supplementary Fig. 1). To efficiently leverage the available data, we propose a two-stage progressive training strategy (Fig. 1b). Through performance evaluation on multiple test sets, we have demonstrated that the two-stage training effectively enhances the feature extraction capabilities of the encoders, thereby improving the performance in predicting pHLA and pTCR binding specificity.

Our model exhibits advantages over previous methods on both pHLA and pTCR binding prediction tasks, and offers at least three notable contributions. First, by integrating both prediction tasks into a unified model, our method enables simultaneous evaluation of the potential in predicting pHLA and pTCR bindings. Such two-faceted assessments provide a more holistic view of antigen immunogenicity than previous methods, offering a new insight into the neoantigen quality for triggering immune response. Moreover, once trained, our model can be independently applied to three prediction tasks: pHLA binding, pTCR binding and HLA-peptide-TCR binding. Second, we devise a two-phase progressive training strategy to make full use of the pHLA and pTCR pairwise binding data available. Our experiments have validated that these two tasks mutually improve each other, by compelling the encoders to extract more expressive features. Furthermore, the virtual adversarial training effectively enhances the model generalizability. Finally, our extensive experiments on multiple independent and external test datasets have verified that the unified model achieved superior performance over current state-of-the-art methods on both prediction tasks. Moreover, the cross-attention scores facilitated the capture of underlying patterns of peptides binding to HLA and TCR molecules.

Results

Performance evaluation on pHLA binding prediction

To evaluate our model performance in predicting pHLA binding, we conducted performance assessment on four datasets: independent test, external test, human papilloma virus (HPV) and neoantigen validation datasets. We compared UnifyImmun against 12 established methods, including NetMHCpan_EL²⁸, NetMHCpan_BA²⁸, ANN³⁸, Pick-Pocket³⁹, SMMPMBEC⁴⁰, SMM⁴¹, NetMHCcons⁴², NetMHCstabpan⁴³ and Consensus⁴⁴, as well as three recently published attention-based methods, TransPHLA²⁶, ACME⁴⁵ and DeepAttentionPan⁴⁶. These competing methods were downloaded as executable packages and run on the same test sets using their recommended parameters. We reported multiple performance metrics, such as area under the receiver operating characteristic curve (AUROC), accuracy, Matthews correlation coefficient (MCC) and F_1 -score (Fig. 2a). To offer more comprehensive evaluation, we also provided other metrics, including precision, recall, area under the precision-recall curve (AUPR) and specificity (Extended Data Fig. 1a).

We first evaluated the performance of UnifyImmun against other competing methods on an independent set, which contained 10% pHLA samples held out from our established benchmark dataset ('Dataset'). The results showed that UnifyImmun remarkably outperformed all other methods across all evaluation metrics (Fig. 2a). In particular, compared with the second-best method, TransPHLA, UnifyImmun achieved at least a 5% improvement in both AUROC and AUPR. To provide a visual presentation of the performance differences, we presented the receiver operative characteristic curves (Fig. 2b) and precision-recall curves (Extended Data Fig. 1b) for all competing methods on the hold-out test set. These curves further validated the superior performance of our proposed method. The UMAP feature visualized that the positive and negative samples separated notably in the latent space (Fig. 2c). To further assess the model's ability to prioritize pHLA bindings, we presented the positive predictive value (PPV) for the top

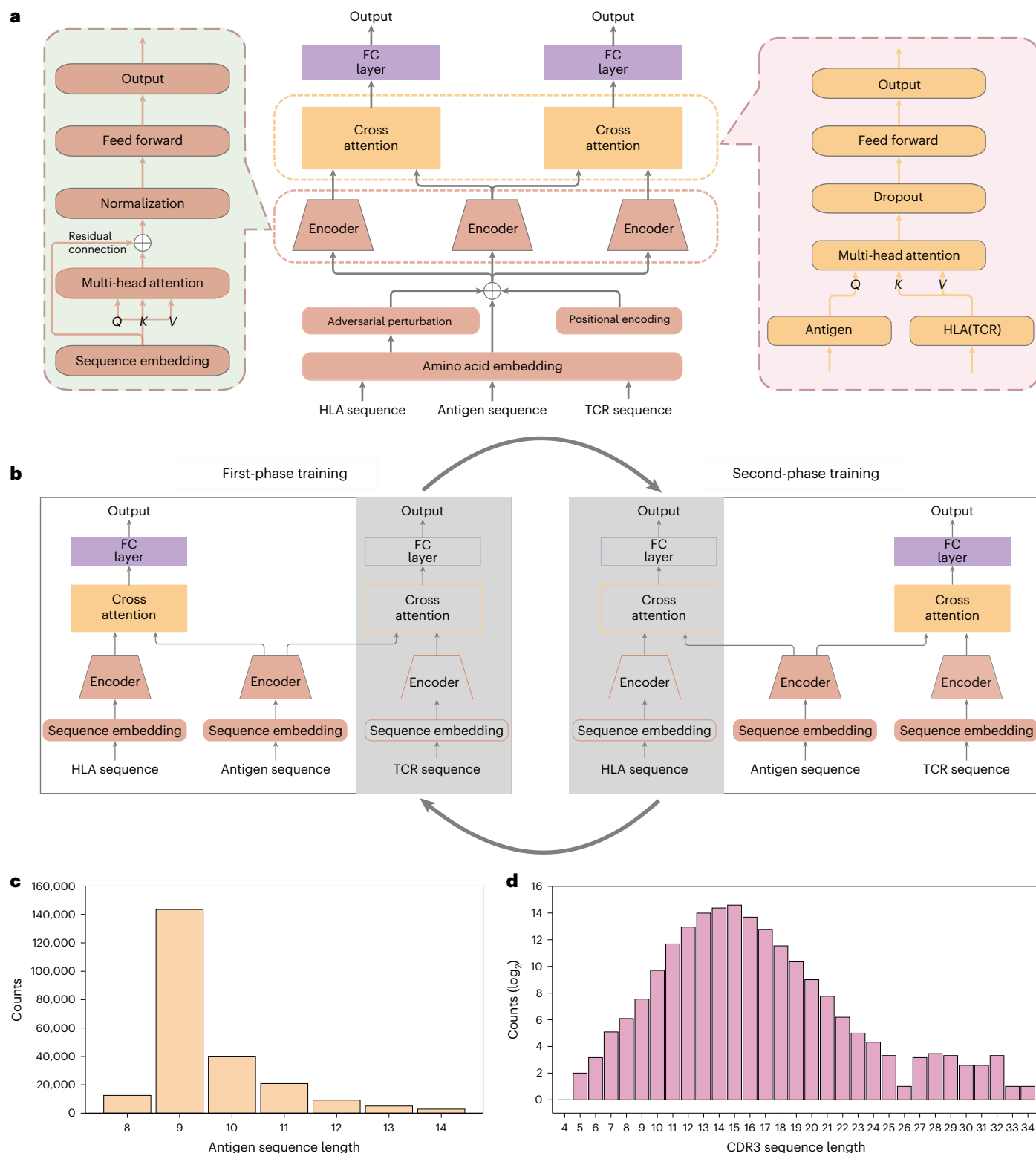


Fig. 1 | Illustrative diagram of UnifyImmun framework and two-phase training strategy, as well as the sequence frequency distributions of the benchmark datasets. a, Architecture of UnifyImmun based on the cross-attention

mechanism. **b,** Two-stage progressive training strategy. **c,d,** Frequency of antigen sequences (c) and TCR CDR3 sequences (d) included in our created benchmark datasets with respect to lengths. FC, fully connected.

100, top 1,000 and top 5,000 predicted positive samples (Fig. 2d). UnifyImmun achieved an impressive 100% PPV for the top 100 predictions and maintained excellent performance above 97% for both the top 1,000 and top 5,000 predictions. In contrast, the other methods did not demonstrate comparable ability in prioritizing pHLA bindings. We also

paid attention to the top five HLA alleles with most bindings, including HLA-B27:05, HLA-A02:01, HLA-A03:01, HLA-B07:02 and HLA-B15:01. Our model achieved the best performance on the HLA-A03:01 allele bound by 8-mer peptides ($n = 385$) with 0.941 AUROC value, followed by 9-mer peptides ($n = 17,658$) with 0.915 AUROC value (Extended Data

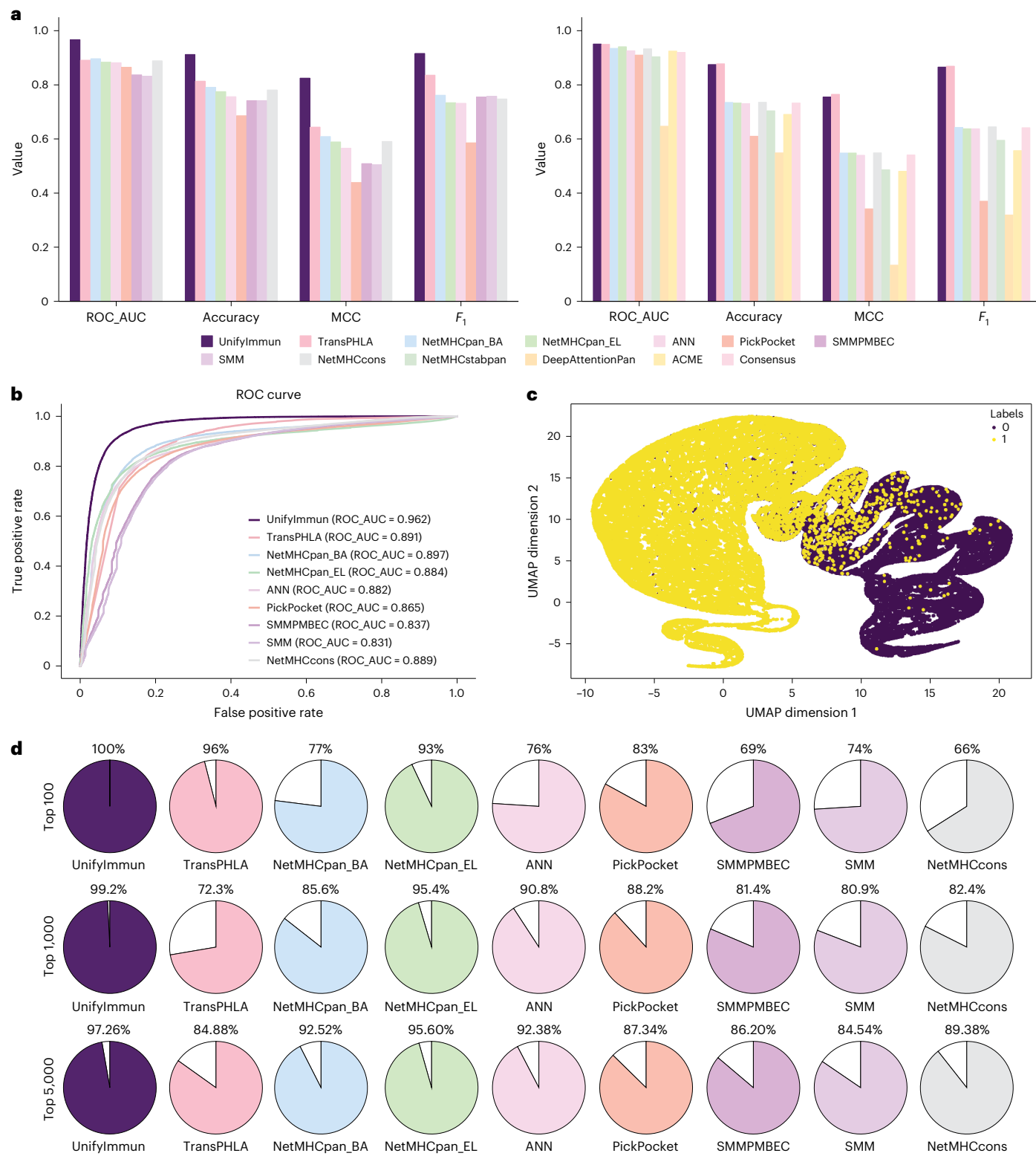


Fig. 2 | Performance evaluation on predicting peptide–HLA binding specificity. **a**, Performance comparison with 12 existing methods on independent (left) and external (right) test datasets, respectively. **b**, ROC curves and AUC values achieved by UnifyImmun and eight competing methods on the hold-out independent test

set. **c**, UMAP feature visualization of peptide–HLA pairs. **d**, PPV for the top 100, top 1,000 and top 5,000 predicted pHLA samples. MCC, Matthews correlation coefficient; ROC, receiver operating characteristic curve.

Table 1). The performance was relatively poor on the HLA-B27:05 allele bound by 14-mer peptides. We also separately checked the performance on the different test subsets split by peptide lengths, and found that UnifyImmun gained the highest AUROC value 0.91 for 9-mer and

11-mer peptides, and the lowest AUROC value 0.88 for 14-mer peptides (Extended Data Table 2).

For objective evaluation, we conducted performance comparison experiments on an external pHLA binding dataset provided by

Anthem⁴⁷. This external set included 103,854 pHLA bindings that cover five HLA alleles and 100,581 distinct peptides, with approximately balanced numbers of positive and negative samples. While TransPHLA exhibited performance advantages on this dataset, UnifyImmum achieved nearly identical performance compared with TransPHLA (Fig. 2a) across all performance metrics. Furthermore, UnifyImmum notably outperformed all other methods except for TransPHLA.

The HPV dataset came from a previous study⁴⁸ that identified 278 experimentally verified pHLA bindings derived from the HPV16 proteins E6 and E7, consisting of peptides ranging from 8 to 11 amino acids in length^{49,50}. We compared UnifyImmum against 15 previous methods on this test set. Because some competing methods cannot accommodate every HLA allele and peptide length, they thereby failed to cover all test samples. UnifyImmum achieved an impressive accuracy rate of 83.8% (Extended Data Fig. 1c). This significantly surpassed the performance of the second-best model, TransPHLA, which correctly identified only 68% of pHLA bindings. The neoantigen validation dataset includes 221 experimentally verified pHLA bindings²⁶, which were collected from non-small-cell lung cancer, melanoma, ovarian cancer and pancreatic cancer in recent studies. On this test set, UnifyImmum achieved 94.1% accuracy (correctly identifying 208 of 221) and actually performed comparably to TransPHLA with 96.4% (Extended Data Fig. 1d). These different types of test sets were complementary in the performance evaluation, so only a method that worked well on all the test sets can demonstrate its superiority. Collectively, the performance comparison experiments on four distinct datasets clearly demonstrated the superior generalization capability of UnifyImmum over previous methods.

UnifyImmum boosts predictive performance of pTCR bindings
To assess the performance in predicting pTCR binding specificity, we conducted performance comparison with four current state-of-the-art methods devised for the task, including PanPep³¹, ERGO2 (ref. 34), pMTnet³² and DLpTCR³³. For PanPep, ERGO2 and pMTnet, we executed their executable codes using their recommended parameters on the same workstation as UnifyImmum. For DLpTCR, we accessed its web server to obtain its predicted results of the test sets. We observed notable differences in the inference efficiency among the evaluated methods. Upon comparing time overhead on our local workstation for four methods (excluding DLpTCR), UnifyImmum exhibited markedly higher inference efficiency compared with PanPep and pMTnet, while being slightly less efficient than ERGO2 (Supplementary Fig. 6).

We initially evaluated the performance of these methods on our established pTCR binding dataset with negative samples generated through random mismatching. On the 10% hold-out independent test set ('Dataset'), we found that UnifyImmum remarkably outperformed all other methods (Fig. 3a,g and Extended Data Fig. 2a,c). Specifically, UnifyImmum achieved AUROC and AUPR values of 0.938 and 0.936, highlighting its exceptional predictive ability in predicting pTCR binding specificity. Among the competing methods, only ERGO2 exhibited moderate performance, with AUROC and AUPR values of 0.704 and 0.747, respectively. Other methods performed close to random guessing, indicating their weak generalizability in predicting pTCR bindings. For specific-length peptides, UnifyImmum achieved the highest area under the curve (AUC) value of 0.95 for 9-mer peptides and the lowest AUC value of 0.87 for 12-mer peptides (Extended Data Table 3).

For further evaluation, we compiled an external test set of pTCR binding pairs from a number of publications, which included 97,043 pTCR pairs spanning 1,239 distinct peptides and 24,856 CDR3 sequences. This external set did not contain any shared peptide with the training set, allowing us to assess the predictive capacity of UnifyImmum towards real-world scenarios beyond the hold-out test set. As expected, UnifyImmum achieved AUROC values of 0.889 and AUPR values of 0.888, significantly outperforming the second-best method, ERGO2, which obtained only about 0.663 AUROC and AUPR values (Fig. 3b,h and Extended Data

Fig. 2b,d). The other three methods exhibited even poorer performance on the external set. We observed even negative MCC values for PanPep and DLpTCR, indicating a high degree of disagreement between their prediction and ground truth. This observation reflected the limitations of the previously published methods, and in turn validated that UnifyImmum achieved superior performance in predicting pTCR binding specificity between unseen peptides and TCR sequences.

To check the ability to prioritize pTCR bindings, we computed the PPV for the top-ranked predicted pTCR samples on the two distinct datasets mentioned above. Specifically, we evaluated the PPV for the top 100, top 1,000 and top 5,000 predictions (Fig. 3d,e). UnifyImmum achieved an impressive 97%, 97.7% and 94.7% PPV values for the top 100, top 1,000 and top 5,000 predictions, respectively. In contrast, the prioritization ability of the other methods was inferior to UnifyImmum. The UMAP feature visualization of pTCR pairs implied that the positive and negative samples separated remarkably in the latent space (Supplementary Fig. 3a,b). It is indeed noteworthy that while the competing methods may exhibit promising results on small datasets, their performance decreased seriously when tested on large-scale datasets. This implies they suffer from weak generalization ability and struggle to adapt to large real-world data scenarios. In contrast, UnifyImmum demonstrated strong robustness across distinct datasets, offering a more dependable and precise tool for predicting pTCR binding specificity.

Moreover, we employed an alternative strategy to generate negative pTCR samples (Methods). This strategy combined random mismatching and an unbound sequence pool, with each contributing 50% of the negative pTCR samples. Following this, we conducted performance evaluation experiments similar to those described above. The experimental results included the performance metrics of our method alongside four competing methods on both the hold-out independent test set and the external test set (Supplementary Fig. 4). While all methods exhibited a decline in performance compared with the dataset with negative samples generated exclusively through random mismatching, our method consistently outperformed the four competing algorithms across various performance metrics, including the PPV for the top 100, 1,000 and 5,000 predicted pTCR bindings. The results strongly demonstrated that our method achieved significantly better generalizability across different datasets whose negative samples were generated using different strategies.

Two-phase progressive training improved model performance
Due to the limited number of HLA–antigen–TCR triplet samples for model training, we devised a two-phase progressive training strategy ('Two-phase progressive training') aimed at effectively leveraging the available pHLA and pTCR pairwise binding data. To validate the performance enhancement from two-phase training, we randomly divided our established benchmark datasets into training and test sets for model training and subsequent performance assessment. This process was independently repeated ten times to account for variations introduced by random data partitioning. We presented the results in boxplots for each training round (Fig. 4). The results showed that the performance of our method was suboptimal for both pHLA and pTCR binding prediction in the absence of alternating training, namely, Round 0. As the number of training rounds progressed, we noticed a significant and steady increase in performance until it stabilized at a notably high level. Specifically, on the pHLA hold-out independent test set, the two-phase training quickly boosted the AUROC and AUPR values (Fig. 4a,b). The one-way analysis of variance (ANOVA) revealed statistically significant differences between the first and last bins for the AUROC and AUPR values (F -test, $P = 4.75 \times 10^{-20}$ and 2.94×10^{-15} , respectively).

For pTCR binding prediction, similar trends can be observed on the independent test set (Fig. 4c,d). As expected, the increasing number of training rounds improved the model's performance on the independent test set. The ANOVA analysis confirmed the statistically significant differences between the first and last bins for the AUROC

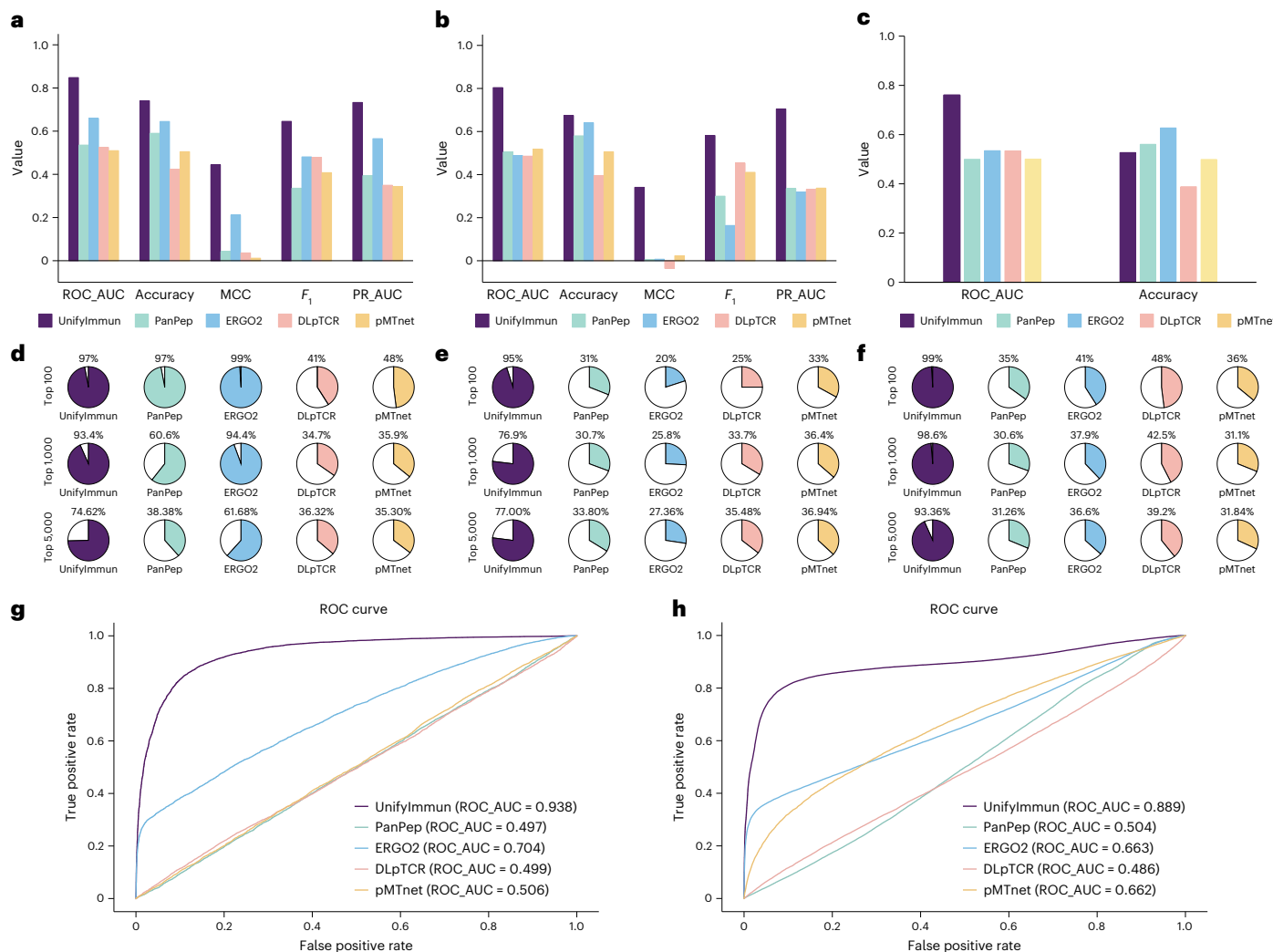


Fig. 3 | Performance evaluation on predicting peptide-TCR binding specificity.

a–c, Performance comparison with four methods on independent (**a**), external (**b**) and COVID-19 (**c**) test sets, respectively. **d–f**, PPV for the top 100 (**d**), top 1,000

(**e**) and top 5,000 (**f**) predicted samples on independent, external and COVID-19 test sets, respectively. **g,h**, ROC curves and AUC values on independent (**g**) and external (**h**) test datasets, respectively.

and AUPR values (*F*-test, $P=0.0167$ and 0.0395 , respectively). Notably, we observed that the variance of the performance metrics was relatively high in the early rounds, but it decreased progressively as the number of training rounds increased. This indicated that the model performance became less affected by random data partitioning as training progressed. These results confirmed that the two-stage progressive training strategy effectively drove the encoders to learn more informative features, thereby achieving more reliable performance.

Cross-attention scores reveal critical peptide sites

We employed the cross-attention mechanism to integrate the features of peptides and HLA/TCR molecules, allowing us to explore whether cross-attention scores reflect the key positions and amino acid types within the peptide that determine its binding affinity to HLA or TCR molecules. For this purpose, we aggregated the cross-attention scores for amino acid type at every position across all peptide sequences. As a result, a higher score indicates its strong influence on the binding affinity to the corresponding receptor. To accommodate peptides of different lengths, we independently generated the heatmaps for peptides ranging from 9 to 14 amino acids in length (Fig. 5 and Supplementary Figs. 7 and 8).

Since 9-mer peptides are the most common, we inspected the heatmaps to uncover important amino acid types and positions. For

pHLA binding, we found remarkably higher attention scores at the second position (P2) and C terminus (Fig. 5a), indicating that these two sites make remarkable contributions to the peptides bound by HLA molecules. Meanwhile, the Leu (L) amino acid consistently received higher attention scores, especially at the two key positions, emphasizing its significance for pHLA binding. For pTCR binding, we also found that the Leu at the second peptide position⁵¹ stands out as the most influential (Fig. 5d). To support the observations of cross-attention heatmaps, we calculated the integrated gradients for each amino acid type at every position within the peptide (Supplementary Figs. 9 and 10). For 9-mer peptides, the integrated gradient heatmaps exhibited high similarity to the attention heatmaps (Fig. 5b,e). For instance, the Leu amino acid at the second position within the peptides emerged as a crucial residue for the binding to both HLA and TCR molecules. We also observed high frequency of the amino acids in these peptide positions (Supplementary Fig. 1d,e). For other length peptides, we also observed that the Leu amino acid at the P2 and C terminus is highlighted in the heatmaps generated from both attention and integrated gradient values. The consistency between the attention scores and the integrated gradient values reinforced the validity of our model and highlighted the crucial role of specific amino acid types and their positions in mediating peptide binding affinity. Furthermore, we calculated the cumulative cross-attention scores for each amino acid type across all positions

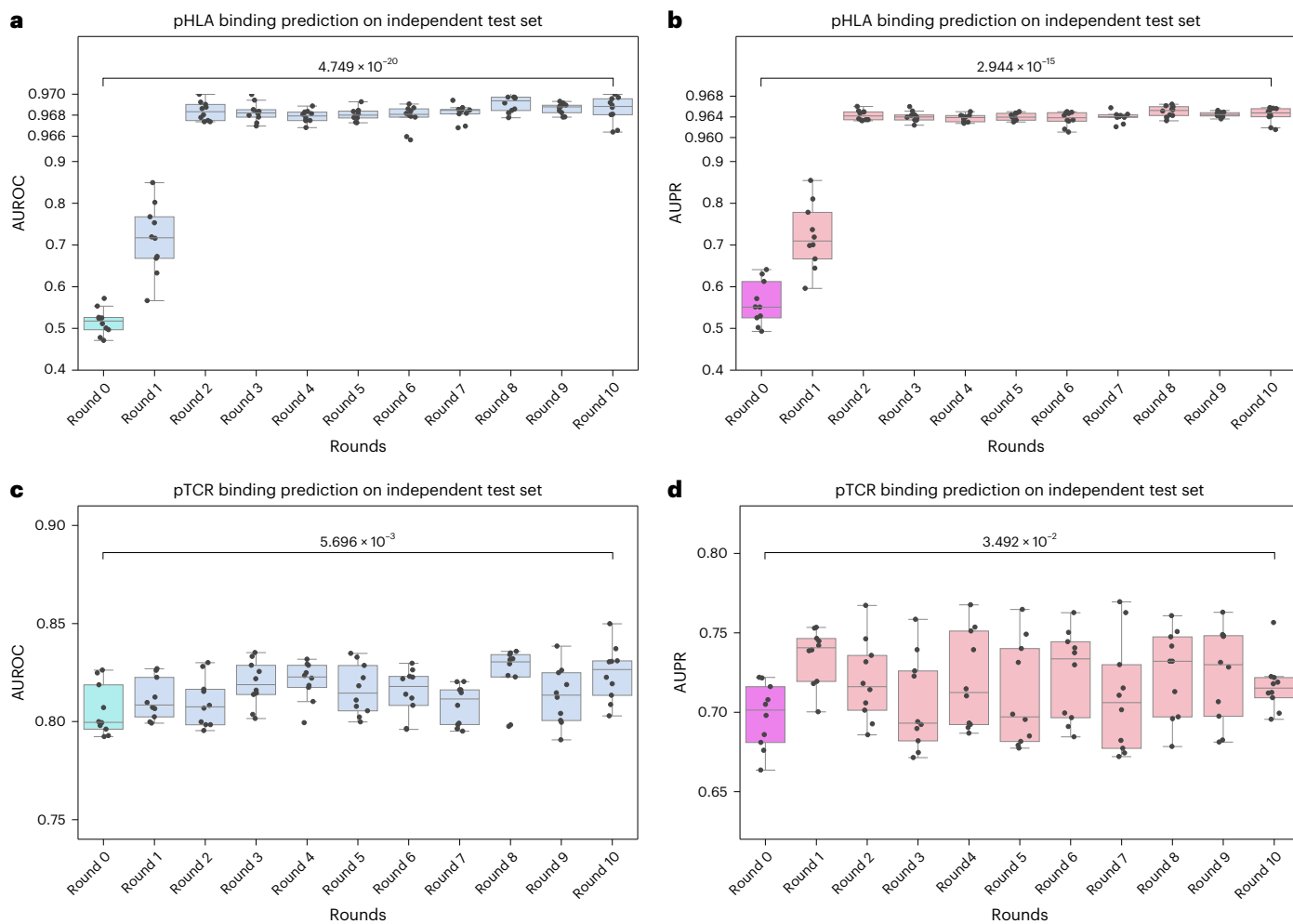


Fig. 4 | Two-phase progressive training improved performance for both pHLA and pTCR binding prediction tasks. a,b, AUROC (a) and AUPR (b) values increased with two-phase training rounds on the pHLA independent test set. **c,d,** AUROC (c) and AUPR (d) values increased with two-phase training rounds on the pTCR independent test set. In all the boxplots, the sample size is 10 for each round, and each point represents the result of a technical replicate by random

data partitioning. The horizontal line within each box represents the median, the box boundaries denote the interquartile range (Q25 to Q75) and whiskers extend to the most extreme data point no more than 1.5 times the interquartile range. The one-sided *F*-test was performed to assess the statistical differences between the two groups connected by a line, with the corresponding *P* values displayed above the respective lines.

within specific-length peptides. The cumulative value reflects the overall importance of specific amino acid types in mediating peptide binding to HLA or TCR. We illustrated the heatmaps generated from the cumulative scores of 20 distinct amino acids in peptides ranging from 8 to 14 amino acids in length (Fig. 5c,f). Clearly, Leu consistently demonstrated high importance in peptides binding to both types of receptors.

To explore the crucial residues in peptide binding to specific HLA alleles, we generated the attention heatmap for the top five HLA alleles with most 9-mer binding peptides, including HLA-A02:01, HLA-A03:01, HLA-B07:01, HLA-B15:01 and HLA-B27:05 (Fig. 5g). It can be observed that the Leu amino acid at the second position significantly affects antigen binding to HLA-A02:01 and HLA-A03:01. For HLA-B15:01 and HLA-B27:05, the Tyr (Y) at the C terminus and Arg (R) at P2 exhibited a dominant role. In fact, several studies have reported the crucial amino acids and their positional preferences in peptide binding to specific HLA alleles. Our heatmaps confirmed these reported residues that exhibited remarkably high scores at their preferential positions. For instance, refs. 52,53 showed that HLA-A1 prefers Asp (D)/Glu (E) at P3 and Tyr(Y) at the C terminus, which was consistently reflected in our heatmap for HLA-A01:01 (Extended Data Fig. 3b). Similarly, other studies have described preferential amino acids for HLA-B8, HLA-B14,

HLA-B27 and HLA-B44, all of which were well-represented in our attention heatmaps^{53–56}. These findings strongly validate the crucial amino acids and their positional preferences in peptide binding to specific HLA alleles as reported by previous studies and uncovered by our methods.

For intuitive visualization of the important sites and amino acids involved in HLA-peptide-TCR binding, we obtained the crystal structure of the TK3 TCR in complex with HLA-B*3501/HPVG (PDB 3MV7) from the PDB database. We extracted the HLA allele, antigen (11-mer) and the CDR3 β chain (11-mer) and predicted the pairwise binding probabilities using UnifyImmun. The results indicated a high binding score between the HLA-B*3501 allele and antigen (0.99), as well as a moderate score between the CDR3 β chain and antigen (0.62). Furthermore, the attention heatmap for this pHLA-TCR complex (Fig. 5h) revealed a significantly high cross-attention score between the eighth amino acid Tyr (Y) of the antigen and the eighth amino acid Gly (G) of the CDR3 β chain. For the CDR3 α chain, we obtained a similar attention heatmap (Extended Data Fig. 3a). Upon careful inspection of the three-dimensional structure (Fig. 5i), we found the hydrogen bonds associated with these two amino acids. This observation indicates their crucial role in the formation of the pTCR complex, despite their distance of 8.77 Å (distance between two C α atoms of two amino acids),

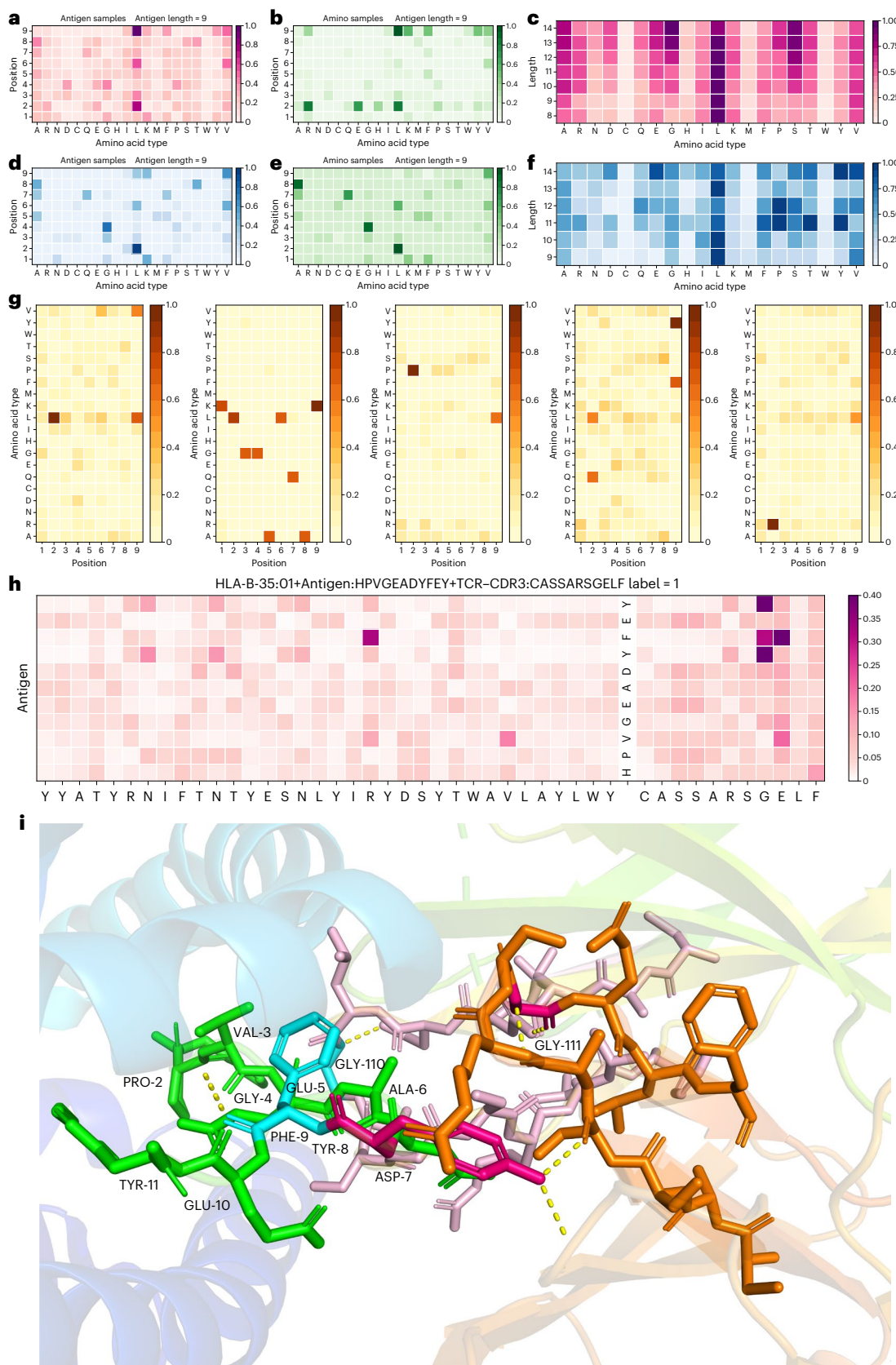


Fig. 5 | Heatmaps generated from cross-attention scores and integrated gradients. **a,b**, Heatmaps of cross-attention scores (**a**) and integrated gradients (**b**) of the amino acid type at each position of 9-mer peptide binding to HLA molecules. **c**, Cumulative attention scores across peptide length of each amino acid type of peptide binding to HLA molecules. **d,e**, Heatmaps of cross-attention scores (**d**) and integrated gradients (**e**) of the amino acid type at each position of

9-mer peptide binding to TCR molecules. **f**, Cumulative attention scores across peptide length of each amino acid type of peptide binding to TCR molecules. **g**, Heatmaps of cross-attention scores for the top five HLA alleles with most 9-mer binding peptides. **h,i**, Attention score-based heatmap (**h**) and three-dimensional structure (**i**) for the TCR complex with HLA-B35:01/HPVG (PDB 3MV7).

which is slightly beyond the conventional contact threshold of 6 Å. We also observed that the ninth amino acid Phe (F) in the antigen received remarkably high cross-attention scores for HLA binding. Consistently, the complex crystal structure showed that Phe is embedded in the HLA binding groove (represented by blue helices) and stabilized through hydrogen bonds (yellow lines). In addition, the heatmaps of two randomly selected pHHLA–TCR complexes (one positive and one negative) revealed that the attention scores in the positive sample were significantly higher than those in the negative sample (Supplementary Fig. 11a,b). In summary, the cross-attention mechanism offers an opportunity to explore the global dependencies between TCR–pHLA interactions, thereby enhancing the interpretability of our model.

High generalizability to COVID-19 pTCR binding prediction

To validate the generalizability of UnifyImmun, we tested its ability to predict the bindings between COVID-19 virus-derived antigens and TCRs. We collected more than 540,000 bindings between antigens derived from COVID-19 virus and human TCRs from the ImmuneCODE database⁵⁷. To demonstrate UnifyImmun's predictive capability for novel peptides, we removed all pTCR samples associated with the shared peptides in the training set, and ensured that all peptides in this test set were unseen in the model training stage. Meanwhile, we generated an equal number of negative samples via random mismatching, thereby creating a million-scale COVID-19 test set. To our knowledge, this is the largest pTCR binding test so far. We compared UnifyImmun with several other methods, including PanPep, ERGO2, DLpTCR and pMTnet. Due to the low efficiency of pMTnet and DLpTCR, they were unable to tackle the million-scale test set within a reasonable time frame. Therefore, we randomly selected 100,000 pairs as their test set for evaluation.

The results illustrated that UnifyImmun achieved an AUROC value of 0.623 (Fig. 3c and Supplementary Fig. 5). In contrast, the other methods obtained AUROC values only slightly above 0.5, which is close to random guessing. Clearly, UnifyImmun outperformed all competitive methods by more than 10% in this unseen peptide context. Furthermore, we computed the PPV values for the top 100, top 1,000 and top 5,000 predictions made by each method. Our model consistently achieved 90% PPV values, remarkably outperforming all the competing methods whose PPV values were always less than 65% (Fig. 3f). In addition, we conducted a performance evaluation on the dataset containing negative pTCR samples generated using the hybrid strategy (Supplementary Fig. 4c,f). The experimental results validated that UnifyImmun consistently outperformed four competing methods across various performance metrics, as well as the PPV for the top 100, 1,000 and 5,000 predicted pTCR bindings. Overall, the significant advantages over previous methods strongly validated the robust generalizability of UnifyImmun, and highlighted its potential for facilitating the development of effective immune-based therapies and vaccines against COVID-19 viruses.

Predicted binding scores correlated with immunotherapy outcomes

The antigen presentation to cytotoxic T cells plays a pivotal role in determining the efficacy of tumour immunotherapy, particularly with immune checkpoint inhibitors. To evaluate the predictive power of UnifyImmun, we conducted correlation analysis on two cancer cohorts: a metastatic melanoma cohort (MM-HLA)⁵⁸ for pHHLA binding, and an advanced melanoma cohort⁵⁹ for pTCR binding (MM-TCR).

The MM-HLA cohort included 110 patients, with each patient harbouring an average of 919 neoantigens. For each patient, we obtained the HLA typing, antigen sequences, immunotherapy responses and clinical outcomes. For the MM-HLA cohort, we applied the response evaluation criteria in solid tumors (RECIST) criteria to categorize the patients into four groups: complete response (CR, $n = 3$), partial response (PR, $n = 14$), stable disease (SD, $n = 12$) and progressive disease

(PD, $n = 76$). We predicted the binding probabilities for all possible HLA–peptide pairs using UnifyImmun and visually represented the predicted results for each patient group. The one-way ANOVA with an *F*-test revealed statistically significant differences in the pHHLA binding affinity between these groups (Fig. 6a). Notably, the PD group demonstrated a highly statistically significant divergence compared with the other patient groups. This observation implied the differences in neoantigen presentation between benefit versus non-benefit patient groups from immunotherapy. Moreover, the patients in the CR group exhibited the prevalence of high-scored neoantigens, while those in the PD group showed many low-scored neoantigens. If the patients were stratified into response ($n = 27$), non-response ($n = 73$) and long survival ($n = 10$) groups according to the standard that progression free survival is less than 180 d but overall survival is more than 2 yr, they exhibited distinct patterns in antigen binding to HLA molecules (Fig. 6c; for details of the violin plots see Supplementary Fig. 12e). As a contrast, we tested TranspHLA and netMHCcons on MM-HLA. The results showed that TranspHLA was not effective enough to statistically distinguish the pHHLA bindings between CR and PR patients in the MM-HLA cohort, as well as between the CR and SD groups (Extended Data Fig. 4a; $P = 0.271$ and 0.682, respectively).

The MM-TCR cohort comprised 29 patients who had received immunotherapy, and each patient underwent TCR sequencing (TCR-seq) and genomic sequencing. Taking the amino acid resulting from a missense mutation as an anchor, we generated all possible 9-mer peptides harbouring this anchor site. After extracting the CDR3 sequences from TCR-seq data, we created all possible peptide–CDR3 pairs for each patient, yielding a total of 81,851,486 pairs. We used UnifyImmun to score the pairs and selected the top 5,000 highest-scoring pairs for each patient. Next, we categorized the patients into CR ($n = 2$), PR ($n = 5$), SD ($n = 9$) and PD ($n = 12$) groups, and plotted the boxplots of the predicted scores for each group (Fig. 6b). The one-way ANOVA revealed statistically significant differences among the groups (*F*-test; Fig. 6b), with the CR and PR groups harbouring pTCR pairs with significantly higher scores than the SD and PD groups. By stratifying the patients into benefit ($n = 13$), non-benefit ($n = 13$) and long-term survival groups ($n = 3$), we found that the patients in the long-term survival group exhibited highly scored pTCR pairs compared with other groups (Supplementary Fig. 12f).

Finally, to confirm the correlation between highly scored pHHLA and pTCR pairs by UnifyImmun and improved clinical outcomes, we conducted survival analysis on two melanoma cohorts (MM-HLA and MM-TCR). We considered the top 2% pHHLA and pTCR pairs as high-confidence bindings, and stratified the patients with such bindings into the high-confidence group, while the remaining patients were placed into the low-confidence group. The survival analysis showed that the high-confidence group exhibited significantly higher overall survival and progression free survival compared with the low-confidence group (Fig. 6c,d and Supplementary Fig. 12a,b). The *P* values were 0.0038 and 0.031 for the two cohorts, respectively. We also found that the MM-TCR cohort patients in the CR and response groups exhibited relatively high antigenic expression levels (Supplementary Fig. 12c,d). These findings suggest that the patients with highly scored pHHLA and pTCR bindings predicted by UnifyImmun benefited more from immunotherapy and yielded favourable clinical outcomes.

Discussion and conclusion

In this study, we introduced UnifyImmun, a unified cross-attention model designed to simultaneously predict the binding specificity of peptides to both HLA and TCR molecules. We have devised a two-phase progressive training strategy through which the two tasks mutually cooperated to improve the performance of each other, by driving the encoders to capture more expressive features that enhance performance. To bolster the model's generalizability, we have incorporated virtual adversarial perturbation into the framework. When

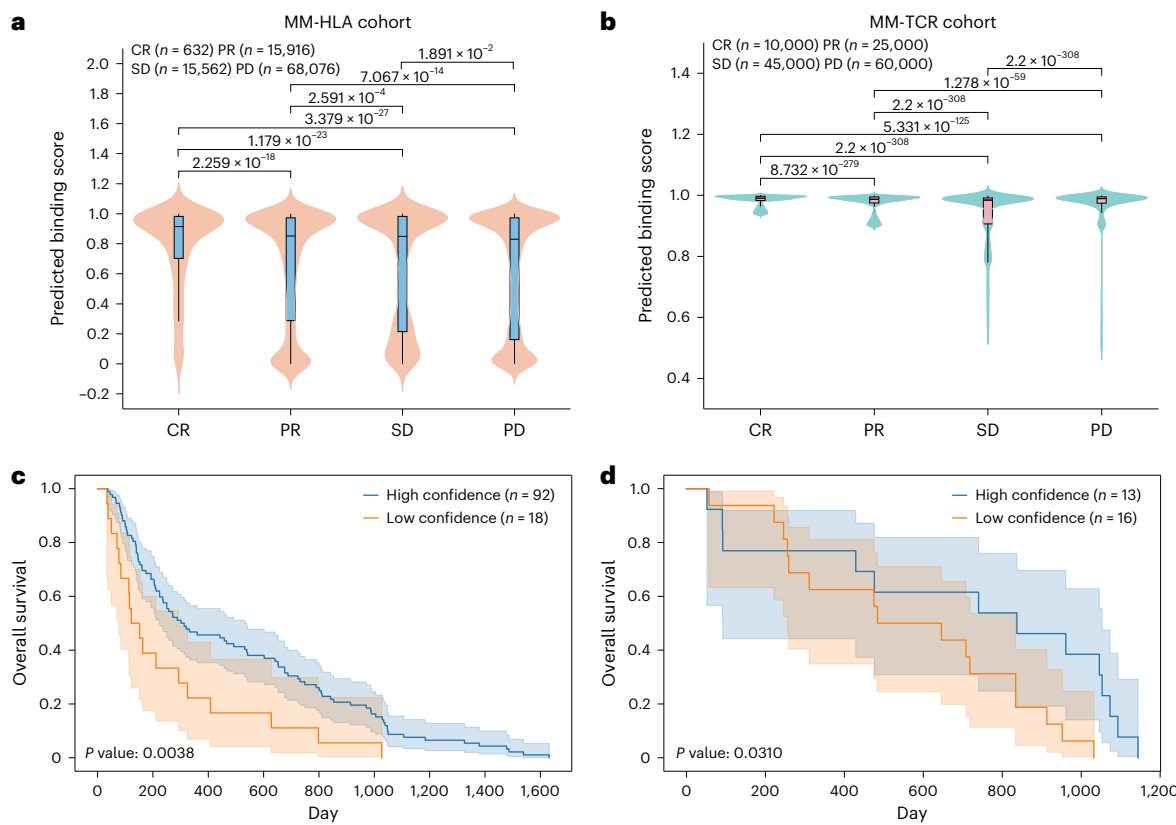


Fig. 6 | Correlation between UnifyImmun predicted binding scores and immunotherapy response and clinical outcomes on two clinical cohorts.

a, Violin plots of predicted pHLA binding scores regarding the different immunotherapy response groups of the MM-HLA cohort with CR ($n = 632$), PR ($n = 15,916$), SD ($n = 15,562$) and PD ($n = 68,076$), respectively. **b**, Violin plots of predicted pTCR binding scores regarding the different immunotherapy response groups of the MM-TCR cohort with CR ($n = 10,000$), PR ($n = 25,000$), SD ($n = 45,000$) and PD ($n = 60,000$), respectively. For the boxplots within the

violin plot, the horizontal line within each box represents the median, the box boundaries denote the interquartile range (Q25 to Q75) and whiskers extend to the most extreme data point no more than 1.5 times the interquartile range. The one-sided F-test was performed to assess the statistical differences between the two groups connected by a line, with the corresponding P values displayed above the respective lines. **c,d**, Survival curves between stratified patient groups with high- and low-confidence antigen binding specificity on MM-HLA (**c**) and MM-TCR (**d**) cohorts, respectively.

benchmarked against over ten previously published methods for pHLA and pTCR binding prediction, our method consistently outperformed them in both tasks on hold-out test sets and multiple external sets. Additionally, the cross-attention scores pinpointed the amino acid sites crucial for peptide binding to receptors.

However, we acknowledge that our method still has some limitations. First, our model integrated the prediction tasks of pHLA and pTCR bindings into a unified framework, offering a more comprehensive evaluation of antigen immunogenicity compared with previous models that only considered individual tasks alone. However, it is important to note that the antigen-induced immune system activation involves a series of cascading biological events¹¹, with a couple of factors influencing the antigen immunogenicity. They include endopeptidase preferences for polypeptide cleavage sites, antigen concentration, stability of pHLA complexes and transporter protein efficiency, all of which affect the degree of immune response activation. While our model marks an essential advancement in the holistic assessment of antigen immunogenicity, it remains a high-level simplification of the actual immune response process.

Second, the currently available TCR CDR3 sequences constitute just a very small fraction of the immense TCR repertoire. This poses a tough challenge for developing method to predict pTCR binding specificity. Although our model can capture underlying patterns for antigen recognition from the TCR sequences, its capacity is still hindered by the scarcity of available data. This problem becomes particularly serious when confronted with unseen peptides in the test set. This might

be the reason why our method showed only moderate performance on the real COVID-19 test set. Fortunately, the remarkable progress in single-cell transcriptome sequencing has led to a significant increase in single-cell RNA sequencing data of T cells, greatly facilitating the acquisition of CDR3 sequences. By leveraging the power of large language models for pretraining, we can extract more expressive and meaningful features from the massive sequences⁶⁰. This would greatly enhance the predictive capabilities of our model to accurately assess the immunogenicity of antigens.

Finally, the currently available training samples are actually biased to certain epitopes and their clonally expanded pairing TCRs. Compared with the vast generation space of unseen peptides, such as neoantigens and exogenous virus peptides, the number of epitopes is very limited. Also, the strategy to generate negative pTCR samples is also biased from normal protein distributions. These issues would lead to overfitting of our model, resulting in unsatisfactory performance on unseen epitopes. Therefore, it is needed to consider a new strategy to generate more generic negative samples, so that we can learn a more robust model.

Methods

Dataset

In this study, we consider only the HLA class I molecules. We created a benchmark dataset^{47,61–63} of pHLA bindings from over ten previous studies (for more details see Supplementary Table 1). After removal of duplicates and abnormal sequences (such as missing values or asterisks), we obtained 410,422 pHLA bindings, spanning 142 HLA alleles

and 279,924 unique peptides. The frequencies of amino acids in the HLA pseudo sequences and peptides bound by HLA molecules are shown in Supplementary Fig. 1a,d,f. The pHLA binding dataset was split into the training set and the hold-out test set by a 9:1 ratio. As a result, the training set contained 322,471 pairs, spanning 139 HLA alleles and 219,744 antigens. The independent test set contained 35,968 pairs, covering 118 HLA alleles and 33,606 antigens. We generated approximately twice the number of negative pHLA samples through two ways: random mismatching and unbound sequence pool. Random mismatching is done by shuffling HLA and peptide sequences and then randomly pairing them. Although this method can result in negative samples containing peptides and HLAs identical to those in the positive samples, potentially introducing negative sample bias⁶⁴, the occurrence or proportion of such false negatives is minimal and can be considered negligible. In contrast, the second way involved retrieving long protein sequences from the Immune Epitope Database (IEDB) immunopeptidomes, which were then randomly segmented into shorter sequences to create an unbound sequence pool. From this pool, sequences were randomly extracted to pair with specific peptides to generate negative samples for each HLA allele. As a result, the negative samples generated by these two methods each composed approximately 50% of the total negative samples.

For each HLA allele, a portion of negative peptides were generated from the segments of the source proteins of IEDB HLA immunopeptidomes. Other negative samples were generated by shuffling the positive HLA and peptide sequences and then randomly mismatched. Although false negative samples may be generated, the possibility and proportions of such samples are very low and can be ignored.

To establish a large-scale benchmark dataset^{23,65–71} of pTCR bindings, we considered both α and β chains of TCR and treated them as single CDR3 sequences, since previous studies have verified that both chains are crucial for antigen recognition^{25,72–76}. By gathering pTCR binding data from a number of previous studies (Supplementary Table 1), we created a pTCR binding dataset with 137,740 pairs, covering 1,488 unique antigens, and 128,169 unique TCR CDR3 sequences. The frequency of amino acids in the TCR CDR3 sequences and peptides bound by TCR molecules are shown in Supplementary Fig. 1b,c,e,g. We employed two strategies to generate pTCR negative samples, thereby constructing three separate pTCR binding datasets for model training and evaluation. The first strategy utilized random mismatching to generate an equal number of negative samples corresponding to the positive samples. The second strategy, termed the hybrid strategy, combined random mismatching and an unbound sequence pool, with each contributing 50% of the total negative samples. Using the hybrid strategy, we established two other datasets, one with 1:1 positive-to-negative sample ratio and another with 1:5 positive-to-negative sample ratio. All datasets were divided into training and test sets at a 9:1 ratio to ensure robust evaluation.

To the best of our knowledge, both the pHLA and the pTCR binding datasets we built are the largest to date.

Sequence embedding

The HLA pseudo sequences have a fixed length of 34 amino acids. Each amino acid is mapped to a 64-dimensional embedding via a character embedding layer. Since the order of amino acids is critical to the protein structure and function, the sine and cosine positional encoding is applied to each position. The amino acid embedding and positional embedding are summed to obtain the sequence embedding. As a result, each HLA pseudo-sequence is represented as a 34×64 matrix.

The antigen peptides are padded to a maximum length of 15 to handle the variable input length, and then each amino acid is mapped to a 64-dimensional embedding. Similarly, the positional encoding is applied to incorporate positional information of each amino acid. After the padding and embedding steps, each peptide is represented as a 15×64 matrix.

All the TCR CDR3 sequences shorter than 34 amino acids are padded to 34, while a small portion of CDR3 sequences exceeding 34 amino acids are truncated. Next, a similar embedding process is applied to each CDR3 sequence, resulting in a 34×64 representation matrix.

Self-attention encoder

The encoder is based on the self-attention mechanism⁷⁷, which has shown exceptional capability in extracting global dependency relationships from protein sequences^{78–80}. The self-attention mechanism learns the attention scores for all possible amino acid pairs within the input sequence. It computes the attention weights from the normalized dot product of query vectors Q and key vectors K followed by a softmax operation, and outputs the weighted sum of the value vectors V by the attention scores. The operations of a self-attention layer written in matrix form are as follows:

$$\text{Attention}(Q, K, V) = \text{softmax}\left(\frac{QK^T}{\sqrt{d_k}}\right)V \quad (1)$$

where d_k is the dimension of the vectors (chosen as 64). Taking HLA as an example, the Q , K and V are all set to its 34×64 embedding matrix. Subsequently, the output of the self-attention block is passed through feed-forward layers: first expanding to 512 dimensions with the rectified linear unit (ReLU) activation function, and then compressing to 64 for a condensed representation. The peptides and TCR encoders share the same network architecture but have independent parameters.

It is important to highlight that we introduce the mask mechanism in calculating the self-attention scores for peptides and CDR3 sequences. Specifically, for the peptides or CDR3 sequences shorter than their respective maximum lengths, we exclude non-amino acid characters from consideration during model training. For this purpose, we assign zero attention scores corresponding to these characters, so that they do not influence the computation of attention scores. In our implementation, the encoder comprises a one-layer, one-head self-attention block.

Cross-attention for feature fusion

The cross-attention mechanism has been demonstrated to effectively capture the intricate relationships and global dependencies between different sequences^{81,82}. Therefore, we leverage the cross-attention mechanism to fuse the feature regarding the interactions between peptide and HLA/TCR molecules. The calculation of cross-attention scores is similar to self-attention. For the fusion of HLA and peptide feature, the HLA embedding matrix acts as the K and V , while the peptide embedding matrix serves as the Q . Subsequently, the V matrix is weighted by the cross-attention scores computed between Q and K . The output of the cross-attention block passes through two feed-forward layers, by which the dimension first rises and then falls. A similar process is applied for the fusion of TCR and peptide features, where TCR embedding acts as K and V matrices, and peptide embedding serves as the Q matrix.

We also employ the mask mechanism when calculating the cross-attention scores, because the mask mechanism greatly reduces the computational overhead and accelerates the model convergence. In our implementation, we adopt one-layer, one-head cross-attention mechanism, as illustrated in Fig. 1.

Prediction of binding specificity

To predict the bindings between peptides and HLA (or TCR) molecules, we flatten the fused matrix of HLA (or TCR)–peptide pairs outputted by the cross-attention block, resulting in a 2,176-dimensional vector (aka 3,464). This vector then passes through three fully connected layers with 256, 64 and 2 nodes, utilizing the ReLU activation function. The final output is obtained via a softmax layer. We adopt cross-entropy as the loss function and use the Adam optimizer with a learning rate of 1×10^{-3} .

The model training is conducted on a CentOS Linux 8.2.2004 (Core) system, equipped with an Intel(R) Xeon(R) Silver 4210R CPU operating at 2.40 GHz, along with a GeForce RTX 4090 GPU and 128 GB of memory. The model is implemented using PyTorch v.2.2.1. On the large-scale benchmark dataset we built, one epoch took about 6 h when the batch size was set to 8,192 (Supplementary Fig. 2). When tested on a set with 100,000 samples, model inference finished within 10 s.

Virtual adversarial training

The virtual adversarial training⁸³ introduces subtle perturbations within the vicinity of the sequence embedding space, rather than directly perturbing the original sequences. The perturbations are oriented towards the direction of loss gradient ascent and are typically generated under L2 norm constraints. This training strategy demands that the model not only minimizes the empirical risk but also minimizes the adversarial loss, making the model less sensitive to slight changes in the input. Formally, the adversarial loss is defined as below:

$$L_{\text{adv}}(x, \theta) = D[p(y|x, \hat{\theta}), p(y|x + r_{\text{adv}}, \theta)], \quad (2)$$

where $r_{\text{adv}} = \arg \max_{r: \|r\| \leq \epsilon} D[p(y|x_*, \hat{\theta}), p(y|x + r)],$

D represents the function that measures the divergence between two distributions, $p(y|x)$ denotes the probability of the model predicting label y given input x and r_{adv} is a virtual adversarial perturbation regarding the input sample x . This perturbation strives to maximize the divergence between $p(y|x_*, \hat{\theta})$ and $p(y|x + r)$ by following the direction of gradient ascent.

We apply adversarial perturbations to the embeddings of all three types of sequences, so that the encoder learns to extract discriminative features. Our ablation experiments have confirmed that virtual adversarial learning indeed improves model performance, as shown in Supplementary Table 2.

Two-phase progressive training

The two-phase progressive training strategy is illustrated in Fig. 1b. In the first phase, the model is trained exclusively on the pHLa pairs, keeping the TCR encoder and the pTCR cross-attention module fixed. This enforces the model to concentrate solely on learning the intricacy of HLA–antigen interactions. In the second phase, the model is trained exclusively using the TCR–peptide pairs, with the HLA encoder and HLA–antigen cross-attention module fixed. The two phases alternate until the model performance converges. Note that throughout the alternating training process, the antigen encoder remains continuously updated and shared between the HLA–antigen and TCR–antigen binding prediction tasks. By iteratively refining the antigen encoder parameters, the model learns to capture the essential information relevant to both HLA and TCR binding, thereby enhancing its overall predictive accuracy.

Model ablation experiments

To validate the contributions of different components, we conducted ablation experiments to assess the performance in predicting pHLa and pTCR bindings. Specifically, we evaluate the attention masking, positional encoding and virtual adversarial perturbation independently. The performance of the ablated models for pHLa and pTCR binding prediction is outlined in Supplementary Tables 2 and 3, respectively.

The results reveal that the removal of any component leads to a decrease in performance. Notably, the removal of virtual adversarial perturbation has the most significant impact, resulting in at least 7% drop in AUROC for both pHLa and pTCR binding predictions. This strongly indicates that virtual adversarial training contributes to the improvement of overall performance and generalization capabilities.

Furthermore, we observed that absence of the attention masking leads to increased computational overhead during the training process. Without the mask, additional computational resources are expended to process the padding sequences, which increases computational cost.

Reporting summary

Further information on research design is available in the Nature Portfolio Reporting Summary linked to this article.

Data availability

The benchmark datasets of the UnifyImmun model are available at GitHub (<https://github.com/hliulab/UnifyImmun>) and via Zenodo at <https://doi.org/10.5281/zenodo.14282419> (ref. 84). The data resources for building the benchmark datasets are detailed in Supplementary Table 1. The external test set and neoantigen test sets for pHLa bindings are available at <https://github.com/a96123155/TransPHLA-AOMP/tree/master/Dataset>. The HPV test set was obtained from the Supplementary Data of ref. 48. The TCR CDR3 sequence, non-synonymous mutations, host gene expression levels and immunotherapy responses of the MM-TCR cohort are available at https://github.com/riazn/bms038_analysis. The HLA alleles, tumour antigen sequences and immunotherapy responses of MM-HLA are available at <https://doi.org/10.1126/science.aad0095>. The published large cohort COVID-19 dataset is available at <https://clients.adaptive-biotech.com/pub/covid-2020>. The 3D crystal complex is available at the PDB with accession number PDB 3MV7. Source data are provided with this paper.

Code availability

The source codes of the UnifyImmun model are available at GitHub (<https://github.com/hliulab/UnifyImmun>) and via Zenodo at <https://doi.org/10.5281/zenodo.14282419> (ref. 84). We have also developed a user-friendly web server that can be freely accessed at <http://hliulab.tech/unifyImmun/>.

References

- Schumacher, T. N. & Schreiber, R. D. Neoantigens in cancer immunotherapy. *Science* **348**, 69–74 (2015).
- Glanville, J. et al. Identifying specificity groups in the T cell receptor repertoire. *Nature* **547**, 94–98 (2017).
- Zhang, J. et al. The combination of neoantigen quality and T lymphocyte infiltrates identifies glioblastomas with the longest survival. *Commun. Biol.* **2**, 135 (2019).
- Yang, K., Halima, A. & Chan, T. A. Antigen presentation in cancer—mechanisms and clinical implications for immunotherapy. *Nat. Rev. Clin. Oncol.* **20**, 604–623 (2023).
- Barry, M. & Bleackley, R. C. Cytotoxic T lymphocytes: all roads lead to death. *Nat. Rev. Immunol.* **2**, 401–409 (2002).
- Raskov, H., Orhan, A., Christensen, J. P. & Gögenur, I. Cytotoxic CD8⁺ T cells in cancer and cancer immunotherapy. *Br. J. Cancer* **124**, 359–367 (2021).
- Weigelin, B. et al. Cytotoxic T cells are able to efficiently eliminate cancer cells by additive cytotoxicity. *Nat. Commun.* **12**, 5217 (2021).
- Rowen, L., Koop, B. F. & Hood, L. The complete 685-kilobase DNA sequence of the human β T cell receptor locus. *Science* **272**, 1755–1762 (1996).
- Fowell, D. J. & Kim, M. The spatio-temporal control of effector T cell migration. *Nat. Rev. Immunol.* **21**, 582–596 (2021).
- Lim, A. R., Rathmell, W. K. & Rathmell, J. C. The tumor microenvironment as a metabolic barrier to effector T cells and immunotherapy. *eLife* **9**, e55185 (2020).
- Chen, D. S. & Mellman, I. Oncology meets immunology: the cancer-immunity cycle. *Immunity* **39**, 1–10 (2013).

12. Yewdell, J. W. & Bennink, J. R. Immunodominance in major histocompatibility complex class I-restricted T lymphocyte responses. *Annu. Rev. Immunol.* **17**, 51–88 (1999).
13. Dunn, G. P., Old, L. J. & Schreiber, R. D. The three Es of cancer immunoediting. *Annu. Rev. Immunol.* **22**, 329–360 (2004).
14. Trowsdale, J. HLA genomics in the third millennium. *Curr. Opin. Immunol.* **17**, 498–504 (2005).
15. Huppa, J. B. et al. TCR-peptide–MHC interactions in situ show accelerated kinetics and increased affinity. *Nature* **463**, 963–967 (2010).
16. Nikolich-Žugich, J., Slifka, M. K. & Messaoudi, I. The many important facets of T-cell repertoire diversity. *Nat. Rev. Immunol.* **4**, 123–132 (2004).
17. Zhang, S.-Q. et al. Direct measurement of T cell receptor affinity and sequence from naive antiviral T cells. *Sci. Transl. Med.* **8**, 341ra77 (2016).
18. Davis, M. M. & Bjorkman, P. J. T-cell antigen receptor genes and T-cell recognition. *Nature* **334**, 395–402 (1988).
19. Krogsgaard, M. & Davis, M. M. How T cells ‘see’ antigen. *Nat. Immunol.* **6**, 239–245 (2005).
20. Chowell, D. et al. Evolutionary divergence of HLA class I genotype impacts efficacy of cancer immunotherapy. *Nat. Med.* **25**, 1715–1720 (2019).
21. Krishna, C., Chowell, D., Gönen, M., Elhanati, Y. & Chan, T. A. Genetic and environmental determinants of human TCR repertoire diversity. *Immun. Ageing* **17**, 26 (2020).
22. Purcell, A. W., Ramarathnam, S. H. & Ternette, N. Mass spectrometry-based identification of MHC-bound peptides for immunopeptidomics. *Nat. Protoc.* **14**, 1687–1707 (2019).
23. Zhang, S.-Q. et al. High-throughput determination of the antigen specificities of T cell receptors in single cells. *Nat. Biotechnol.* **36**, 1156–1159 (2018).
24. Kula, T. et al. T-scan: a genome-wide method for the systematic discovery of T cell epitopes. *Cell* **178**, 1016–1028 (2019).
25. Hudson, D., Fernandes, R. A., Basham, M., Ogg, G. & Koohy, H. Can we predict T cell specificity with digital biology and machine learning? *Nat. Rev. Immunol.* **23**, 511–521 (2023).
26. Chu, Y. et al. A transformer-based model to predict peptide–HLA class I binding and optimize mutated peptides for vaccine design. *Nat. Mach. Intell.* **4**, 300–311 (2022).
27. O'Donnell, T., Rubinsteyn, A., Bonsack, M., Riemer, A. & Hammerbacher, J. MHCflurry: open-source class I MHC binding affinity prediction. *Cell Syst.* **7**, 129–132 (2018).
28. Reynisson, B., Alvarez, B., Paul, S., Peters, B. & Nielsen, M. NetMHCpan-4.1 and NetMHCIIpan-4.0: improved predictions of MHC antigen presentation by concurrent motif deconvolution and integration of MS MHC eluted ligand data. *Nucleic Acids Res.* **48**, W449–W454 (2020).
29. Haoyang, Z. & Gifford, D. K. DeepLigand: accurate prediction of MHC class I ligands using peptide embedding. *Bioinformatics* **35**, i278–i283 (2019).
30. Cheng, J., Bendjama, K. & Rittner, K. et al. BERTMHC: improved MHC-peptide class II interaction prediction with transformer and multiple instance learning. *Bioinformatics* **37**, 4172–4179 (2021).
31. Gao, Y. et al. Pan-peptide meta learning for T-cell receptor–antigen binding recognition. *Nat. Mach. Intell.* **5**, 236–249 (2023).
32. Lu, T. et al. Deep learning-based prediction of the T cell receptor–antigen binding specificity. *Nat. Mach. Intell.* **3**, 864–875 (2021).
33. Xu, Z. et al. DLpTCR: an ensemble deep learning framework for predicting immunogenic peptide recognized by T cell receptor. *Brief. Bioinform.* **22**, bbab335 (2021).
34. Springer, I., Tickotsky, N. & Louzoun, Y. Contribution of T cell receptor alpha and beta CDR3, MHC typing, V and J genes to peptide binding prediction. *Front. Immunol.* **12**, 664514 (2021).
35. Weber, A., Born, J. & Martínez, M. R. Titan: T-cell receptor specificity prediction with bimodal attention networks. *Bioinformatics* **37**, i237–i244 (2021).
36. Fang, Y., Liu, X. & Liu, H. Attention-aware contrastive learning for predicting T cell receptor–antigen binding specificity. *Brief. Bioinform.* **23**, bbac378 (2022).
37. Meysman, P. et al. Benchmarking solutions to the T-cell receptor epitope prediction problem: Immrep22 workshop report. *Immunoinformatics (Amst.)* **9**, 100024 (2023).
38. Andreatta, M. & Nielsen, M. Gapped sequence alignment using artificial neural networks: application to the MHC class I system. *Bioinformatics* **32**, 511–517 (2016).
39. Zhang, H., Lund, O. & Nielsen, M. The PickPocket method for predicting binding specificities for receptors based on receptor pocket similarities: application to MHC-peptide binding. *Bioinformatics* **25**, 1293–1299 (2009).
40. Kim, Y., Sidney, J., Pinilla, C., Sette, A. & Peters, B. Derivation of an amino acid similarity matrix for peptide:MHC binding and its application as a Bayesian prior. *BMC Bioinform.* **10**, 394 (2009).
41. Peters, B. & Sette, A. Generating quantitative models describing the sequence specificity of biological processes with the stabilized matrix method. *BMC Bioinformatics* **6**, 132 – 132 (2005).
42. Karosiene, E., Lundsgaard, C., Lund, O. & Nielsen, M. NetMHCcons: a consensus method for the major histocompatibility complex class I predictions. *Immunogenetics* **64**, 177–186 (2012).
43. Rasmussen, M. et al. Pan-specific prediction of peptide-MHC class I complex stability, a correlate of T cell immunogenicity. *J. Immunol.* **197**, 1517–1524 (2016).
44. Moutaftsi, M. et al. A consensus epitope prediction approach identifies the breadth of murine T CD8+ cell responses to vaccinia virus. *Nat. Biotechnol.* **24**, 817–819 (2006).
45. Hu, Y. et al. ACME: pan-specific peptide-MHC class I binding prediction through attention-based deep neural networks. *Bioinformatics* **35**, 4946–4954 (2019).
46. Jin, J. et al. Deep learning pan-specific model for interpretable MHC-I peptide binding prediction with improved attention mechanism. *Proteins* **89**, 866–883 (2021).
47. Mei, S. et al. Anthem: a user customised tool for fast and accurate prediction of binding between peptides and HLA class I molecules. *Brief. Bioinform.* **22**, bbaa415 (2021).
48. Bonsack, M. et al. Performance evaluation of MHC class-I binding prediction tools based on an experimentally validated MHC-peptide binding data set. *Cancer Immunol. Res.* **7**, 719–736 (2019).
49. Wells, D. K. et al. Key parameters of tumor epitope immunogenicity revealed through a consortium approach improve neoantigen prediction. *Cell* **183**, 818–834 (2020).
50. Wang, G. et al. INeo-Epp: a novel T-cell HLA class-I immunogenicity or neoantigenic epitope prediction method based on sequence-related amino acid features. *BioMed Res. Int.* **2020**, 5798356 (2020).
51. Parker, K. C. et al. Sequence motifs important for peptide binding to the human MHC class I molecule, HLA-A2. *J. Immunol.* **149**, 3580–3587 (1992).
52. DiBrino, M. et al. HLA-A1 and HLA-A3 T cell epitopes derived from influenza virus proteins predicted from peptide binding motifs. *J. Immunol.* **151**, 5930–5935 (1993).
53. DiBrino, M. et al. Endogenous peptides with distinct amino acid anchor residue motifs bind to HLA-A1 and HLA-B8. *J. Immunol.* **152**, 620–631 (1994).

54. DiBrino, M. et al. The HLA-B14 peptide binding site can accommodate peptides with different combinations of anchor residues. *J. Biol. Chem.* **269**, 32426–32434 (1994).
55. Parker, K. C., Biddison, W. E. & Coligan, J. E. Pocket mutations of HLA-B27 show that anchor residues act cumulatively to stabilize peptide binding. *Biochemistry* **33**, 7736–7743 (1994).
56. DiBrino, M. et al. Identification of the peptide binding motif for HLA-B44, one of the most common HLA-B alleles in the Caucasian population. *Biochemistry* **34**, 10130–10138 (1995).
57. Nolan, S. et al. A large-scale database of T-cell receptor beta (TCR β) sequences and binding associations from natural and synthetic exposure to SARS-CoV-2. Preprint at Research Square (2020).
58. Van Allen, E. M. et al. Genomic correlates of response to CTLA-4 blockade in metastatic melanoma. *Science* **350**, 207–211 (2015).
59. Riaz, N. Tumor and microenvironment evolution during immunotherapy with nivolumab. *Cell* **171**, 934–949.e16 (2017).
60. Fang, X., Yu, C., Tian, S. & Liu, H. A large language model for predicting T cell receptor-antigen binding specificity. In Proc. IEEE International Conference on Bioinformatics and Biomedicine (BIBM) 1489–1492 (2024).
61. Reche, P. A., Zhang, H., Glutting, J.-P. & Reinherz, E. L. EPIMHC: a curated database of MHC-binding peptides for customized computational vaccinology. *Bioinformatics* **21**, 2140–2141 (2005).
62. Bhasin, M., Singh, H. & Raghava, G. P. S. MHCDBN: a comprehensive database of MHC binding and non-binding peptides. *Bioinformatics* **19**, 665–666 (2003).
63. Rammensee, H.-G., Bachmann, J., Emmerich, N. P. N., Bachor, O. A. & Stevanović, S. SYFPEITHI: database for MHC ligands and peptide motifs. *Immunogenetics* **50**, 213–219 (1999).
64. Dens, C., Laukens, K., Bittremieux, W. & Meysman, P. The pitfalls of negative data bias for the T-cell epitope specificity challenge. *Nat. Mach. Intell.* **5**, 1060–1062 (2023).
65. Bagaev, D. V. et al. VDJdb in 2019: database extension, new analysis infrastructure and a T-cell receptor motif compendium. *Nucleic Acids Res.* **48**, D1057–D1062 (2020).
66. Vita, R. et al. The Immune Epitope Database (IEDB): 2018 update. *Nucleic Acids Res.* **47**, D339–D343 (2019).
67. Heikkilä, N. et al. Human thymic T cell repertoire is imprinted with strong convergence to shared sequences. *Mol. Immunol.* **127**, 112–123 (2020).
68. Zhang, W. et al. PIRD: Pan Immune Repertoire Database. *Bioinformatics* **36**, 897–903 (2020).
69. Gilson, M. K. et al. BindingDB in 2015: a public database for medicinal chemistry, computational chemistry and systems pharmacology. *Nucleic Acids Res.* **44**, D1045–D1053 (2016).
70. Dines, J. N. et al. The ImmuneRACE study: a prospective multicohort study of immune response action to COVID-19 events with the ImmuneCODE™ open access database. Preprint at medRxiv 2020–08 (2020).
71. Tickotsky, N., Sagiv, T., Prilusky, J., Shifrut, E. & Friedman, N. McPAS-TCR: a manually curated catalogue of pathology-associated T cell receptor sequences. *Bioinformatics* **33**, 2924–2929 (2017).
72. Zhao, X. et al. Tuning T cell receptor sensitivity through catch bond engineering. *Science* **376**, eabf5282 (2022).
73. Carter, J. A. et al. Single T cell sequencing demonstrates the functional role of $\alpha\beta$ TCR pairing in cell lineage and antigen specificity. *Front. Immunol.* **10**, 1516 (2019).
74. Emerson, R. O. et al. Immunosequencing identifies signatures of cytomegalovirus exposure history and HLA-mediated effects on the T cell repertoire. *Nat. Genet.* **49**, 659–665 (2017).
75. Leem, J., de Oliveira, S. H. P., Krawczyk, K. & Deane, C. M. STCRDab: the structural T-cell receptor database. *Nucleic Acids Res.* **46**, D406–D412 (2018).
76. Mayer, A. & Callan Jr, C. G. Measures of epitope binding degeneracy from T cell receptor repertoires. *Proc. Natl Acad. Sci. USA* **120**, e2213264120 (2023).
77. Vaswani, A. et al. Attention is all you need. In *Advances in Neural Information Processing Systems* Vol. 30 (eds Guyon, I. et al.) 5998–6008 (Curran Associates, 2017).
78. Madani, A. et al. Large language models generate functional protein sequences across diverse families. *Nat. Biotechnol.* **41**, 1099–1106 (2023).
79. Brandes, N., Ofer, D., Peleg, Y., Rappoport, N. & Linial, M. ProteinBERT: a universal deep-learning model of protein sequence and function. *Bioinformatics* **38**, 2102–2110 (2022).
80. Rives, A. et al. Biological structure and function emerge from scaling unsupervised learning to 250 million protein sequences. *Proc. Natl Acad. Sci. USA* **118**, e2016239118 (2021).
81. Honda, S., Koyama, K. & Kotaro, K. Cross attentive antibody-antigen interaction prediction with multi-task learning. In *2021 ICML Workshop on Computational Biology* (2020).
82. Dens, C., Laukens, K., Meysman, P. & Bittremieux, W. A cross-attention transformer encoder for paired sequence data. Preprint at bioRxiv 2023–12 (2023).
83. Miyato, T., Dai, A. M. & Goodfellow, I. J. Adversarial training methods for semi-supervised text classification. In *5th International Conference on Learning Representations* (Poster) (2017).
84. Yu, C., Fang, X., Tian, S. & Liu, H. A unified cross-attention model for predicting antigen binding specificity to both HLA and TCR molecules. Zenodo <https://doi.org/10.5281/zenodo.14282419> (2024).

Acknowledgements

This work was supported by the National Natural Science Foundation of China (grant nos. 62072058 and 62372229) and the Natural Science Foundation of Jiangsu Province (grant no. BK20231271).

Author contributions

H.L. and C.Y. conceptualized the idea. C.Y. implemented the model. C.Y. and X.F. collected the data and conducted the experiments. C.Y. and S.T. plotted figures. H.L. and C.Y. prepared the manuscript. H.L. revised the manuscript. H.L. supervised the research.

Competing interests

The authors declare no competing interests.

Additional information

Extended data is available for this paper at <https://doi.org/10.1038/s42256-024-00973-w>.

Supplementary information The online version contains supplementary material available at <https://doi.org/10.1038/s42256-024-00973-w>.

Correspondence and requests for materials should be addressed to Hui Liu.

Peer review information *Nature Machine Intelligence* thanks Alexandre Reuben, Dong Xu and the other, anonymous, reviewer(s) for their contribution to the peer review of this work.

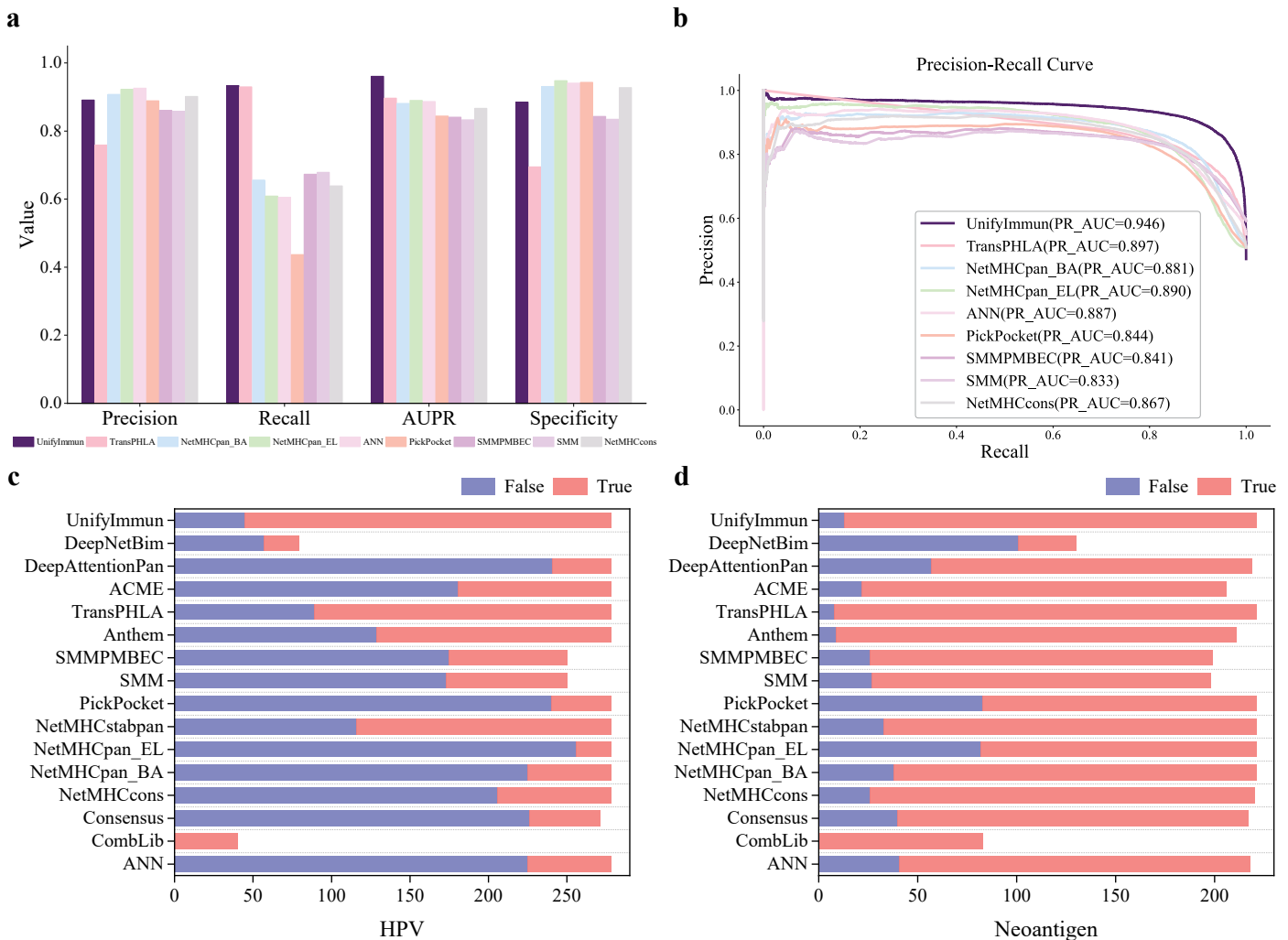
Reprints and permissions information is available at www.nature.com/reprints.

Publisher's note Springer Nature remains neutral with regard to jurisdictional claims in published maps and institutional affiliations.

Springer Nature or its licensor (e.g. a society or other partner) holds exclusive rights to this article under a publishing agreement with

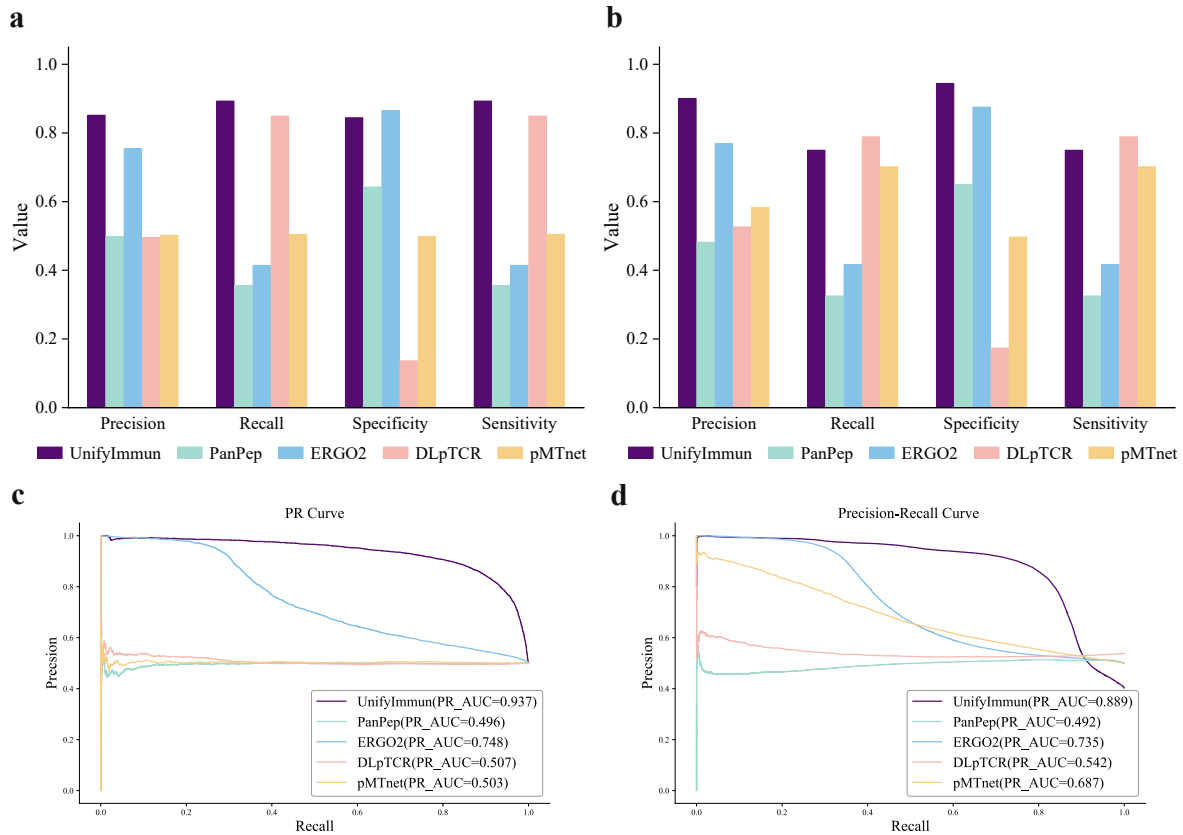
the author(s) or other rightsholder(s); author self-archiving of the accepted manuscript version of this article is solely governed by the terms of such publishing agreement and applicable law.

© The Author(s), under exclusive licence to Springer Nature Limited 2025



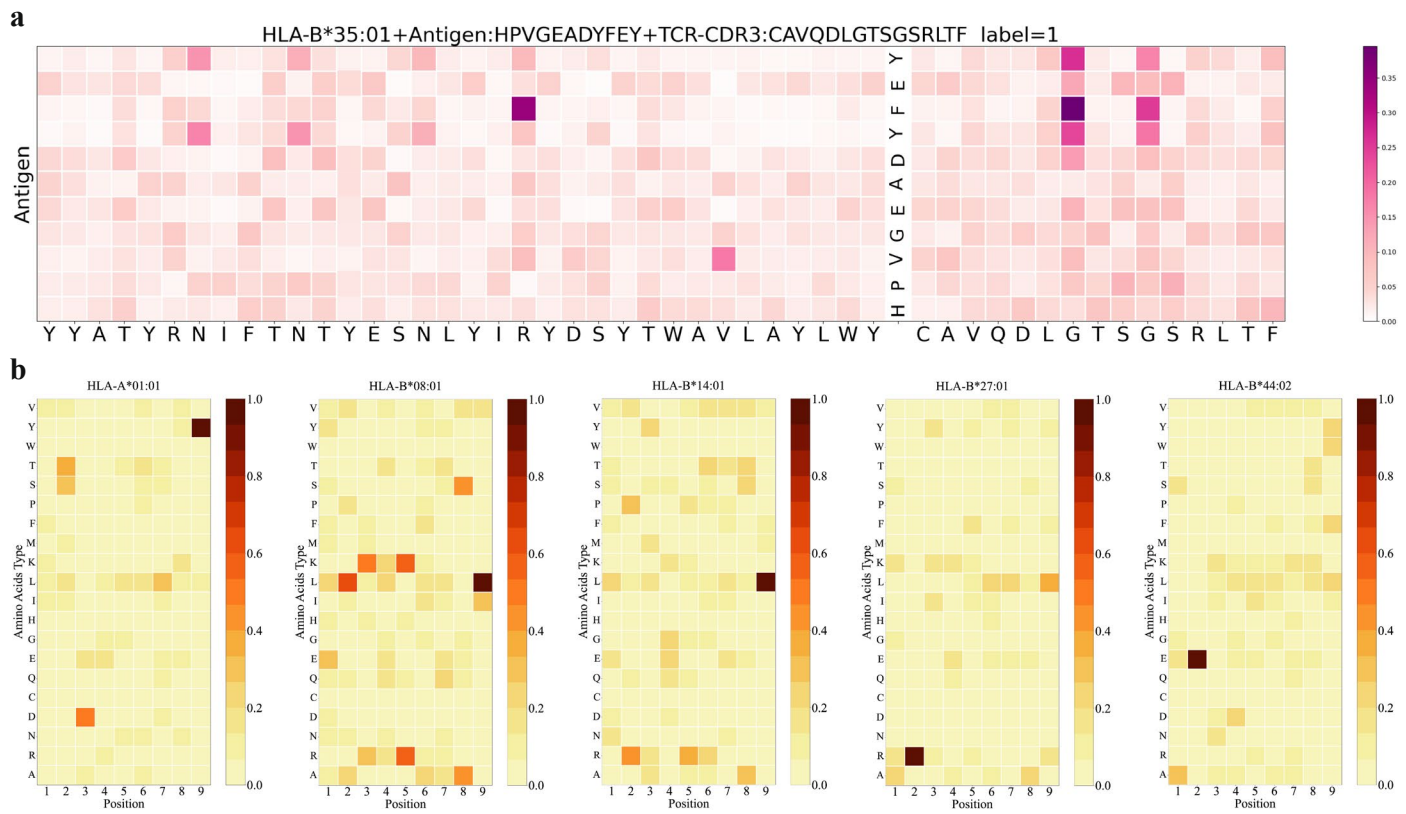
Extended Data Fig. 1 | Additional performance metrics for predicting pHLA binding specificity. (a) Performance comparison with eight other models on the hold-out independent test set. (b) Precision-Recall curves and AUPR values

achieved by UnifyImmun and eight comparative methods on the hold-out independent test set. (c-d) Performance comparison of UnifyImmun with fifteen other models on the HPV dataset and Neoantigen dataset.

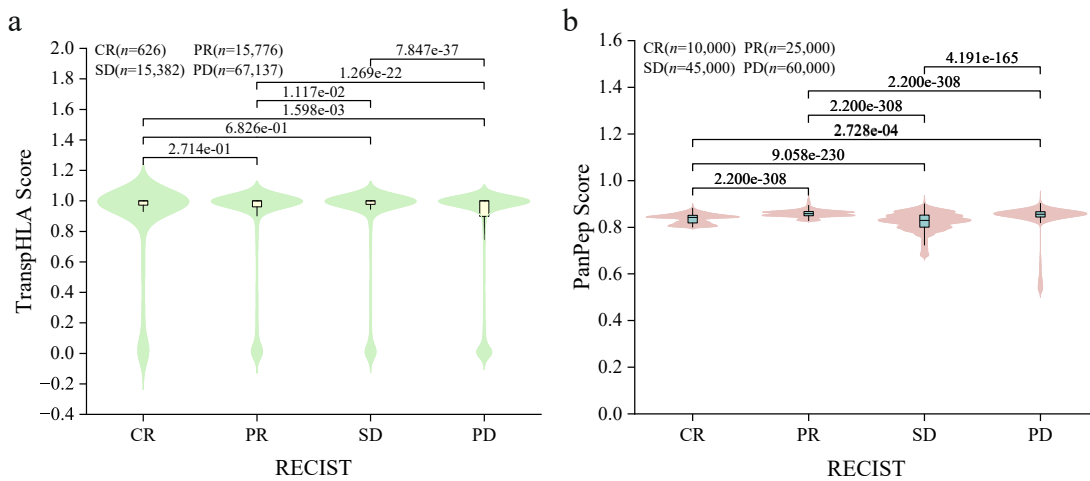


Extended Data Fig. 2 | Additional performance metrics for predicting pTCR binding specificity. (a-b) Additional performance comparison with four methods on independent test set, external test set, respectively. (c,d) PR curves

and AUPR values achieved by UnifyImmun compared to four methods on the independent test set and external test set.



Extended Data Fig. 3 | Heatmaps based on cross-attention scores for 3MV7 complex and pHLA heatmaps. (a) Heatmap based on attention scores for the TCR CDR3 α chain complex with HLA-B*35:01/HPVG (PDB ID: 3MV7). (b) Additional attention heatmaps stratified by HLA alleles.



Extended Data Fig. 4 | Violinplots of predicted pHLA and pTCR binding scores of different immunotherapy response groups two cohorts. (a) Violinplots of predicted pHLA binding scores by TranspHLA in MM-HLA cohort with different RECIST groups, with CR (n=626), PR (n=15,776), SD (n=15,382), and PD (n=67,137), respectively. (b) Violinplots of predicted pTCR binding scores by PanPep in MM-TCR cohort with different RECIST groups, with CR (n=10,000), PR (n=25,000), SD (n=45,000), and PD (n=60,000), respectively. For the boxplots within the

violin plot, the horizontal line within each box represents the median, the box boundaries denote the interquartile range (Q25 to Q75), and whiskers extend to the most extreme data point no more than 1.5 times the interquartile range. The one-sided F-test was performed to assess the statistical differences between the two groups connected by a line, with the corresponding p-values displayed above the respective lines.

Extended Data Table 1 | Performance on the test subsets regarding top five HLA alleles with most bindings to peptides

| HLA | Length | Counts | AUC | ACC | MCC | F1 | TP | FP | TN | FN |
|---------|--------|--------|-------|-------|-------|-------|-------|------|------|-----|
| B*07:02 | 9 | 10015 | 0.881 | 0.912 | 0.771 | 0.941 | 6973 | 492 | 2160 | 390 |
| B*15:01 | 9 | 10465 | 0.875 | 0.923 | 0.728 | 0.953 | 8265 | 340 | 1389 | 471 |
| B*27:05 | 9 | 17011 | 0.656 | 0.765 | 0.406 | 0.847 | 11071 | 3402 | 1938 | 600 |
| A*03:01 | 9 | 17658 | 0.915 | 0.961 | 0.845 | 0.977 | 14702 | 406 | 2266 | 284 |
| A*02:01 | 9 | 20164 | 0.759 | 0.896 | 0.536 | 0.940 | 16531 | 1156 | 1538 | 939 |

Extended Data Table 2 | Performance for predicting pHHLA bindings on the test subsets split by peptide length

| Peptide Length | Counts | AUC | ACC | MCC | F1 | AUPR | FN | FP | TP | TN |
|----------------|--------|------|------|------|------|------|-------|-------|--------|--------|
| 8 | 33338 | 0.91 | 0.91 | 0.82 | 0.90 | 0.84 | 1134 | 1865 | 13106 | 17233 |
| 9 | 468819 | 0.89 | 0.89 | 0.78 | 0.89 | 0.83 | 19219 | 33668 | 211439 | 204493 |
| 10 | 118778 | 0.90 | 0.89 | 0.79 | 0.89 | 0.83 | 4381 | 8129 | 50472 | 55796 |
| 11 | 56041 | 0.91 | 0.90 | 0.80 | 0.89 | 0.82 | 1816 | 3606 | 21203 | 29416 |
| 12 | 23195 | 0.90 | 0.89 | 0.78 | 0.87 | 0.78 | 644 | 1825 | 8148 | 12578 |
| 13 | 13067 | 0.90 | 0.89 | 0.77 | 0.84 | 0.74 | 313 | 1142 | 3933 | 7679 |
| 14 | 6928 | 0.88 | 0.87 | 0.73 | 0.82 | 0.70 | 176 | 731 | 2041 | 3980 |
| 15 | 54 | 0.5 | 0.98 | 0 | 0 | 0.02 | 1 | 0 | 0 | 53 |

Extended Data Table 3 | Performance for predicting pTCR bindings on the test subsets split by peptide length

| Peptide Length | Counts | AUC | ACC | MCC | F1 | AUPR | FN | FP | TP | TN |
|----------------|--------|------|-------|------|------|------|-----|-----|------|------|
| 9 | 11445 | 0.95 | 0.89 | 0.78 | 0.89 | 0.95 | 738 | 521 | 4887 | 5299 |
| 10 | 3783 | 0.93 | 0.878 | 0.74 | 0.87 | 0.91 | 269 | 224 | 1594 | 1696 |
| 11 | 1580 | 0.91 | 0.82 | 0.65 | 0.83 | 0.93 | 211 | 76 | 720 | 573 |
| 12 | 892 | 0.87 | 0.74 | 0.47 | 0.63 | 0.80 | 183 | 50 | 202 | 457 |
| 13 | 1582 | 0.92 | 0.83 | 0.67 | 0.84 | 0.91 | 178 | 90 | 682 | 632 |
| 14 | 1176 | 0.91 | 0.83 | 0.64 | 0.87 | 0.94 | 115 | 83 | 641 | 337 |
| 15 | 1442 | 0.93 | 0.85 | 0.67 | 0.78 | 0.87 | 144 | 75 | 382 | 841 |

Reporting Summary

Nature Portfolio wishes to improve the reproducibility of the work that we publish. This form provides structure for consistency and transparency in reporting. For further information on Nature Portfolio policies, see our [Editorial Policies](#) and the [Editorial Policy Checklist](#).

Statistics

For all statistical analyses, confirm that the following items are present in the figure legend, table legend, main text, or Methods section.

n/a Confirmed

- The exact sample size (n) for each experimental group/condition, given as a discrete number and unit of measurement
- A statement on whether measurements were taken from distinct samples or whether the same sample was measured repeatedly
- The statistical test(s) used AND whether they are one- or two-sided
Only common tests should be described solely by name; describe more complex techniques in the Methods section.
- A description of all covariates tested
- A description of any assumptions or corrections, such as tests of normality and adjustment for multiple comparisons
- A full description of the statistical parameters including central tendency (e.g. means) or other basic estimates (e.g. regression coefficient) AND variation (e.g. standard deviation) or associated estimates of uncertainty (e.g. confidence intervals)
- For null hypothesis testing, the test statistic (e.g. F , t , r) with confidence intervals, effect sizes, degrees of freedom and P value noted
Give P values as exact values whenever suitable.
- For Bayesian analysis, information on the choice of priors and Markov chain Monte Carlo settings
- For hierarchical and complex designs, identification of the appropriate level for tests and full reporting of outcomes
- Estimates of effect sizes (e.g. Cohen's d , Pearson's r), indicating how they were calculated

Our web collection on [statistics for biologists](#) contains articles on many of the points above.

Software and code

Policy information about [availability of computer code](#)

Data collection All data are collected from public repository via Chrome browser, no custom software is used.

Data analysis Python3.10, PyTorch 2.1, PyMOL3.1, Visio2023, Origin2024

For manuscripts utilizing custom algorithms or software that are central to the research but not yet described in published literature, software must be made available to editors and reviewers. We strongly encourage code deposition in a community repository (e.g. GitHub). See the Nature Portfolio [guidelines for submitting code & software](#) for further information.

Data

Policy information about [availability of data](#)

All manuscripts must include a [data availability statement](#). This statement should provide the following information, where applicable:

- Accession codes, unique identifiers, or web links for publicly available datasets
- A description of any restrictions on data availability
- For clinical datasets or third party data, please ensure that the statement adheres to our [policy](#)

The data resources for building the benchmark datasets are detailed in the Table S1 of supplementary file. The external test set and neoantigen test sets for pHLA bindings are available at: <https://github.com/a96123155/TransPHLA-AOMP/tree/master/Dataset>. The HPV test set was obtained from the Supplementary data of ref \cite{bonsack2019performance}. The TCR CDR3 sequence, non-synonymous mutations, host gene expression levels and immunotherapy responses of MM-TCR cohort are available at https://github.com/riazn/bms038_analysis. The HLA alleles, tumor antigen sequences, and immunotherapy responses of MM-HLA are

available at <https://www.science.org/doi/10.1126/science.aad0095>. The HLA alleles, tumor antigen sequences, and immunotherapy responses of UC-HLA cohort are available at <https://journals.plos.org/plosmedicine/article?id=10.1371/journal.pmed.1002309>. The published large cohort COVID-19 dataset is available at <https://clients.adaptivebiotech.com/pub/covid-2020>. The 3D crystal complex is available at PDB (<https://www.rcsb.org>) with accession number 3MV7.

Human research participants

Policy information about [studies involving human research participants and Sex and Gender in Research](#).

| | |
|-----------------------------|---|
| Reporting on sex and gender | No information related to sex or gender was collected. |
| Population characteristics | No human research participant was recruitment. |
| Recruitment | All data sets used in this study were collected from public repository or previously published papers, no human research participant was recruitment. |
| Ethics oversight | No human research participant was recruitment, so no ethics was needed. |

Note that full information on the approval of the study protocol must also be provided in the manuscript.

Field-specific reporting

Please select the one below that is the best fit for your research. If you are not sure, read the appropriate sections before making your selection.

Life sciences Behavioural & social sciences Ecological, evolutionary & environmental sciences

For a reference copy of the document with all sections, see nature.com/documents/nr-reporting-summary-flat.pdf

Life sciences study design

All studies must disclose on these points even when the disclosure is negative.

| | |
|-----------------|---|
| Sample size | For the statistical tests used in the extended application to immunotherapy cohort, the clinical data is obtained from previously published paper. The sample size of each group is determined by the patients' response to treatment according to RECIST criteria. For statistical tests used to verify two-phase progressive training improve model performance, we repeat the training and test for 10 times to avoid the results by chance. For each test, we ensure that the total sample size is more than 20 |
| Data exclusions | No data was excluded. |
| Replication | For statistical tests used to verify two-phase progressive training improve model performance, we repeat the training and test for 10 times to avoid any results induced by chance. For each repeat, we randomly partition the dataset into training and test set by 9:1 ratio. |
| Randomization | For the statistical tests used in the extended application to immunotherapy cohort, the clinical data is obtained from previously published paper. The sample size of each group is determined by the patients' response to treatment according to RECIST criteria. There is no randomization related to this work. |
| Blinding | For the statistical tests used in the extended application to immunotherapy cohort, the clinical data is obtained from previously published paper. There is no blinding related to this work. |

Reporting for specific materials, systems and methods

We require information from authors about some types of materials, experimental systems and methods used in many studies. Here, indicate whether each material, system or method listed is relevant to your study. If you are not sure if a list item applies to your research, read the appropriate section before selecting a response.

Materials & experimental systems

| | |
|-------------------------------------|--|
| n/a | Involved in the study |
| <input checked="" type="checkbox"/> | <input type="checkbox"/> Antibodies |
| <input checked="" type="checkbox"/> | <input type="checkbox"/> Eukaryotic cell lines |
| <input checked="" type="checkbox"/> | <input type="checkbox"/> Palaeontology and archaeology |
| <input checked="" type="checkbox"/> | <input type="checkbox"/> Animals and other organisms |
| <input checked="" type="checkbox"/> | <input type="checkbox"/> Clinical data |
| <input checked="" type="checkbox"/> | <input type="checkbox"/> Dual use research of concern |

Methods

| | |
|-------------------------------------|---|
| n/a | Involved in the study |
| <input checked="" type="checkbox"/> | <input type="checkbox"/> ChIP-seq |
| <input checked="" type="checkbox"/> | <input type="checkbox"/> Flow cytometry |
| <input checked="" type="checkbox"/> | <input type="checkbox"/> MRI-based neuroimaging |